UNIVERSITY OF CALIFORNIA
Santa Barbara

Adaptive Spatial Multiplexing for Millimeter-Wave Communication Links

A Dissertation submitted in partial satisfaction
of the requirements for the degree of

Doctor of Philosophy

in

Electrical and Computer Engineering

by

Colin Sheldon

Committee in Charge:

Professor Mark Rodwell, Chair

Professor Larry Coldren

Professor Upamanyu Madhow

Professor Umesh Mishra

Professor Patrick Yue

September 2009

The Dissertation of
Colin Sheldon is approved:

Professor Larry Coldren

Professor Upamanyu Madhow

Professor Umesh Mishra

Professor Patrick Yue

Professor Mark Rodwell, Committee Chairperson

September 2009

Adaptive Spatial Multiplexing for Millimeter-Wave Communication Links

by

Colin Sheldon

Acknowledgements

I would like to thank my advisor, Professor Mark Rodwell. His guidance and expertise in circuit and system design have made this dissertation possible. His passion and professionalism in academic research set an example I aspire to match as I embark on my professional career.

I would like to thank the members of Professor Rodwell's and Professor Madhow's research groups for their support and assistance with the wireless experiments. In particular, I would like to thank Dr. Munkyo Seo and Eric Torkildson for their contributions to the hardware prototypes presented in this dissertation.

Curriculum Vitæ
Colin Sheldon

Education

2009	Doctor of Philosophy in Electrical and Computer Engineering, University of California, Santa Barbara, CA
2006	M.S. in Electrical and Computer Engineering, University of California, Santa Barbara, CA
2004	ScB in Electrical Engineering, Brown University, Providence, RI

Experience

2005 – 2009	Graduate Research Assistant, Department of Electrical and Computer Engineering, University of California, Santa Barbara, CA
2004 – 2005	Teaching Assistant, Department of Electrical and Computer Engineering, University of California, Santa Barbara, CA
2003 – 2004	Teaching Assistant, Division of Engineering, Brown University, Providence, RI
2003 – 2004	Engineering Intern, Areté Associates, Arlington, VA

Fields of Study

Millimeter-wave communication systems, RF circuit design, and coherent optical communication systems.

Publications

C. Sheldon, M. Seo, E. Torkildson, U. Madhow, and M. Rodwell, "Adaptive Spatial Multiplexing for Millimeter-Wave Communication Links," *IEEE Trans. Microwave Theory Tech.*, submitted.

C. Sheldon, M. Seo, E. Torkildson, M. Rodwell, and U. Madhow, "Four-Channel Spatial Multiplexing Over a Millimeter-Wave Line-of-Sight Link," *IEEE - MTTS International Microwave Symposium (IMS)*, June 2009.

C. Sheldon, E. Torkildson, M. Seo, C.P. Yue, M. Rodwell, and U. Madhow, "Spatial Multiplexing Over a Line-of-Sight Millimeter-Wave MIMO Link: A Two-Channel Hardware Demonstration at 1.2Gbps Over 41m Range," *European Conference on Wireless Technology*, Oct. 2008.

C. Sheldon, E. Torkildson, M. Seo, C.P. Yue, U. Madhow, and M. Rodwell,, "A 60GHz Line-of-Sight 2x2 MIMO Link Operating at 1.2Gbps," *IEEE International Symposium on Antennas and Propagation*, July 2008.

L.A. Johansson, C. Sheldon, A. Ramaswamy, and M. Rodwell, "Time-Sampled Linear Optical Phase Demodulation," *Coherent Optical Technologies and Applications (COTA) Topical Meeting*, July 2008.

A. Ramaswamy, L.A. Johansson, J. Klamkin, H.F. Chou, C. Sheldon, M.J. Rodwell, L.A. Coldren, J.E. Bowers, "Integrated Coherent Receivers for High-Linearity Microwave Photonic Links," *IEEE Journal of Lightwave Technology*, vol. 26, no. 1, pp. 209-216, Jan. 2008.

A. Ramaswamy, L.A. Johansson, J. Klamkin, C. Sheldon, H.F. Chou, M.J. Rodwell, L.A. Coldren, and J.E. Bowers, "Coherent Receiver Based on a Broadband Optical Phase-Lock Loop," *Optical Fiber Communication Conference*, Mar. 2007.

M. Rodwell, Z. Griffith, N. Parthasarathy, E. Lind, C. Sheldon, S.R. Bank, U. Singisetti, M. Urteaga, K. Shinohara, R. Pierson, and P. Rowell, "Developing Bipolar Transistors for Sub-mm-Wave Amplifiers and Next-Generation (300 GHz) Digital Circuits," *IEEE Device Research Conference (DRC)*, June 2006.

M. Rodwell, Z. Griffith, V. Paidi, N. Parthasarathy, C. Sheldon, U. Singisetti, M. Urteaga, R. Pierson, P. Rowell, and B. Brar, "InP HBT Digital ICs and MMICs in the 140-220 GHz band," *Joint 30th International Conference on Infrared and Millimeter Waves and 13th International Conference on Terahertz Electronics*, Sept. 2005.

Abstract

Adaptive Spatial Multiplexing for Millimeter-Wave Communication Links

Colin Sheldon

Spatial multiplexing for wireless communication systems is typically used at low GHz carrier frequencies in non Line-of-Sight environments. This dissertation considers adaptive spatial multiplexing for Line-of-Sight wireless links at millimeter-wave carrier frequencies. This architecture provides increased data capacity without increasing the channel bandwidth. The aggregate system data rate scales linearly with the number of transmitter and receiver antenna pairs.

System theory and link sensitivity to non ideal installations, multipath signal propagation, and atmospheric refraction are considered. Channel separation hardware implementation considerations are analyzed.

Initial work with a two-element prototype using IF channel separation is presented. This prototype achieved 1.2 Gb/s operation over a 6 m indoor link and similar performance for an outdoor link with a 41 m link range.

A scalable baseband system architecture is proposed and demonstrated for an indoor link operating over a 5 m link range. The spatially multiplexed channels were separated at the receiver using broadband adaptive analog I/Q vector signal

processing. A control loop continuously tuned the channel separation electronics to correct for changes with time in either the propagation environment or the system components. The four-channel 60 GHz hardware prototype achieved an aggregate system data rate of 2.4 Gb/s.

Contents

List of Figures

List of Tables

Chapter 1

Introduction

Radio links employing spatial multiplexing provide increased communication link data capacity without increased channel bandwidth. Research in this area has focused primarily on non line-of-sight links operating at low GHz carrier frequencies (e.g., IEEE 802.11n wireless local area networks in the WiFi bands) [2–4] and aggregate data rates below 1 Gb/s. In contrast, the millimeter (mm) wave MIMO system presented in this dissertation can support spatial multiplexing in Line-of-Sight (LOS) environments with moderate antenna separation, while taking advantage of the wide swathes of unlicensed and semi-unlicensed bandwidth available at 60 GHz and 71-95 GHz (E-band).

Spatial multiplexing requires that the receive array responses to each transmit antenna are strongly distinct. The receiver can then apply spatial processing

to separate out the data channels sent by each transmit element. For spatially multiplexed links using linear arrays of a fixed total length, the maximum number of spatially multiplexed channels varies as the inverse of carrier wavelength λ; for rectangular arrays the maximum number of channels varies as $1/\lambda^2$. If the dimensions of the transmitter and receiver are fixed, then a significant advantage in spatial multiplexing gain is obtained by operating at higher carrier frequencies.

The mm-wave MIMO technique described in this dissertation can significantly enhance the already high data rates demonstrated over these bands. Data rates exceeding 10 Gb/s have been demonstrated over a link range on the order of 1 km at a carrier frequency beyond 100 GHz [5, 6]. A 6 Gb/s link operating in the 81-86 GHz band has been reported [7].

Commercially available E-band links currently support data rates up to 1.5 Gb/s [8,9]. Commercial interest in multi-gigabit mm-wave links has been spurred by recent advances in mm-wave Si IC design. Both 60 GHz and E-band ICs [10–16] have been demonstrated in Si IC technologies. Integrated mm-wave phased-array ICs have been demonstrated in both CMOS and SiGe technologies [17–22]. NEC has recently demonstrated transmitter and receiver ICs capable of operating at 2.6 Gb/s using a 60 GHz carrier [23, 24]. A 6 Gb/s direct conversion transceiver has been recently demonstrated at the University of Toronto [25]. Recent Si

IC [26–28] and wireless system [5,6] results demonstrate the potential for wireless links operating beyond 100 GHz.

As an example of a potential application of mm-wave MIMO, consider an outdoor LOS link using 5 GHz of E-band spectrum (e.g., 81-86 GHz). QPSK transmission with 25% excess bandwidth yields a data rate of 8 Gb/s. Four-fold spatial multiplexing over a range of 1 km yields a rate of 32 Gb/s, and can be obtained using a 2×2 rectangular array of antennas with inter-element spacing of approximately one meter. Using dual polarization for an additional two-fold multiplexing yields a data rate of 64 Gb/s. E-band last mile links can become true alternatives to optical fiber links, even using small robust constellations such as QPSK.

Another potential application uses LOS spatial multiplexing for an indoor 60 GHz link for streaming uncompressed HDTV between a cable set-top box and a television. Using QPSK with 25% excess bandwidth over 3 GHz of unlicensed spectrum, a system can attain a data rate of 4.8 Gb/s. Two-fold spatial multiplexing yields a data rate of 9.6 Gb/s, which is enough to support uncompressed HDTV even as screen sizes scale up. Over a 10 m range, this requires an inter-antenna spacing on the order of 10 cm, which is feasible given the size of television displays and cable T.V. converters. Further multiplexing gains could be obtained by using dual polarization [29].

SiBeam has recently introduced chipsets capable of sending 4 Gb/s over 10 m using a 60 GHz carrier [30]. The system employs beamsteering to exploit non line-of-sight communication in the presence of objects between the transmitter and receiver. Transmitter and receiver modules are entering the market with a cost of approximately $800 per pair [31]. The capacity of this link could be increased by employing spatial multiplexing.

Spatial multiplexing over LOS wireless links has been the subject of several theoretical studies. Analysis has shown that LOS links are robust to small errors in antenna positioning and alignment [32–37]. However, the series of mm-wave MIMO prototypes built at UCSB [38–40] provide the first demonstrations of this concept at mm-wave carrier frequencies. It is only at mm-wave frequencies that large LOS spatial multiplexing gains can be obtained with reasonable array dimensions.

A key innovation of the wireless system architecture presented in this dissertation is the decoupling of the spatial processing for channel separation from other receiver tasks, such as synchronization and demodulation. This allows the system to adapt the spatial processing slowly (to respond to slow channel variations) even as the data channels are scaled up to multi-gigabit speeds. Once channel separation is achieved, each data channel is processed separately for demodulation. In particular, the systems presented in this dissertation implement spatial

channel separation using analog circuits, thus avoiding the high-rate sampling and quantization required for digital signal processing of the high-bandwidth mm-wave signals.

This dissertation presents experimental results from a mm-wave MIMO system using a 2-element linear array at each end with a manually tuned channel separation network placed at the receiver IF frequency [38, 39]. This prototype was tested in both indoor and outdoor environments with link ranges of 6 m and 41 m, respectively. The system had an aggregate data rate of 1.2 Gb/s.

Results from a second prototype using a channel separation network operating at baseband are presented. The prototype used a 4-element linear array at each end, with automatically tuned baseband channel separation [40]. Experimental results are reported for an indoor link operating in an office environment. Channels were separated by converting the received signals to baseband and forming linear combinations of their I and Q components, an approach which more readily scales to a large number of channels and compact IC implementation. The channel separation hardware was continuously and adaptively tuned under closed-loop digital control. Control loop signals were derived by monitoring low frequency (< 100 kHz) pilot tones added to the individual transmitter data signals.

The following chapter presents the system theory for LOS spatial multiplexing and an analysis of the system sensitivity to non ideal link installations, multi-

path signal propagation, and atmospheric refraction. Chapter 3 analyzes several methods for implementing the channel separation network hardware required to separate channels at the receiver. An analysis of additional required receiver functions and sample link configurations are presented. Detailed descriptions of the hardware prototypes and experimental results are presented in Chapter 4 and Chapter 5.

Chapter 2

Line-of-Sight Spatial Multiplexing

This chapter presents an analysis of line-of-sight wireless links employing spatial multiplexing. The motivation for the work presented in this dissertation is presented in Section 2.1. Section 2.2 demonstrates that line-of-sight wireless links can be analyzed using the principles of diffraction limited optics. Section 2.3 presents the theory of line-of-sight spatial multiplexing and proposes a mathematical framework for further analysis. A link sensitivity analysis is described in Section 2.4.

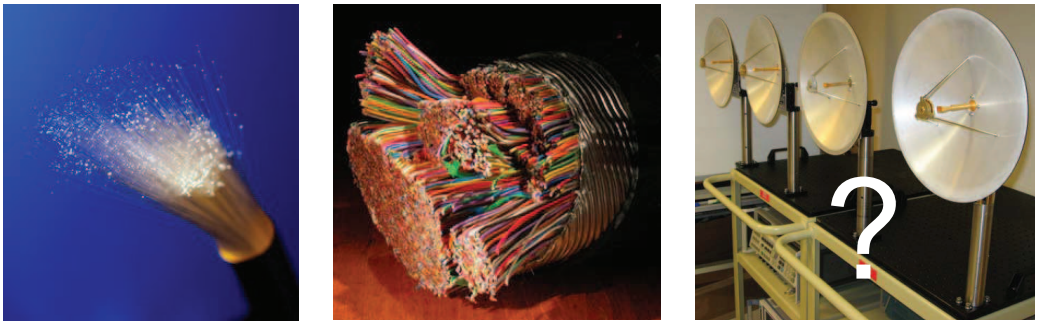

Figure 2.1: Parallel communication links

2.1 Towards 100 Gb/s Wireless Links

Commercial wireless link currently operate at speeds up to approximately 4 Gb/s [30]. A wireless communication system capable of 100 Gb/s would represent an improvement of two orders of magnitude over existing state of the art wireless links.

Parallel links (Figure 2.1) are a simple method for increasing aggregate system data rates and are easily realized for guided wave communication links (optical fiber, cable, etc.). This principle has been applied to commercial wireless products, notably products using the IEEE 802.11n wireless local area network standard in the WiFi bands [2–4]. However, these links operate in non line-of-sight environments using low GHz carrier frequencies and are limited to aggregate system data rates well 1 Gb/s.

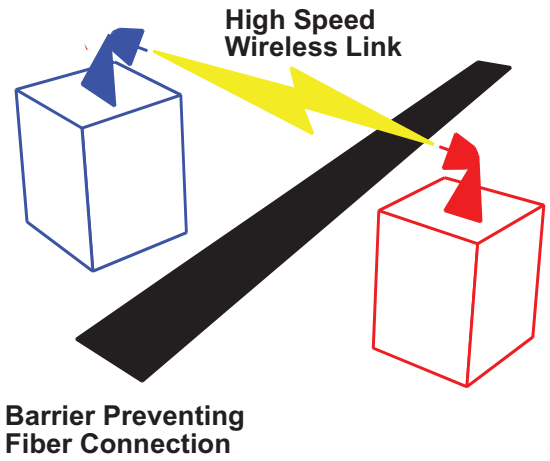

Figure 2.2: High-Speed Line-of-Sight wireless link

New system architectures are needed to build wireless links capable of achieving 100 Gb/s operation. Millimeter-wave carrier frequencies offer an attractive alternative to low GHz carrier operation because of the wide swathes of unlicensed and semi-unlicensed bandwidth available at 60 GHz and 71-95 GHz (E-band).

Line-of-Sight wireless links operating at 100 Gb/s have several potential applications. These links could serve as a wireless bridge for fiber links. They could be used to bridge locations where laying fiber is difficult or expensive (Figure 2.2). 100 Gb/s line-of-sight links could serve as temporary high speed links for the media at sporting events, etc. High Speed line-of-sight links could be used as backbone links for future broadband Wireless Local Area Networks. These links

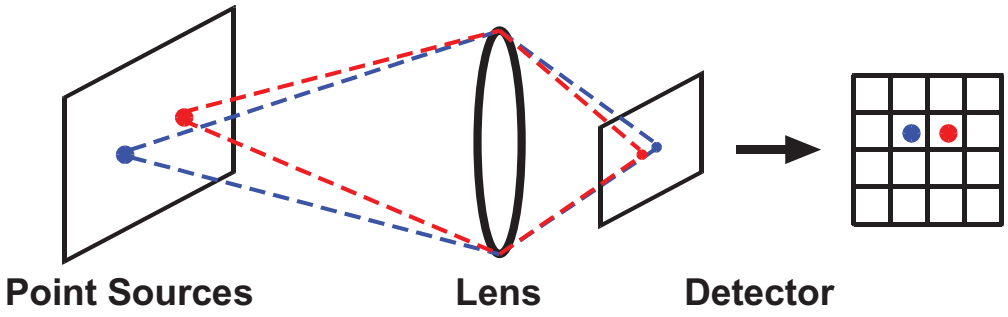

Figure 2.3: Digital video camera

also offer a simple solution for secure building to building high speed wireless connections.

This dissertation seeks to answer the following question: Can parallel links using free space propagation at millimeter-wave carrier frequencies achieve 100 Gb/s aggregate system data rates for line-of-sight wireless links?

2.2 Digital Video Camera: Optics Approach

Digital video camera operation is based on the principles of diffraction limited optics (Figure 2.3). The angular resolution, θ, of a camera is given by

$$\sin(\theta) \cong \theta \cong 1.22 \cdot \frac{\lambda}{D}, \tag{2.1}$$

where λ is wavelength and D is the diameter of the camera's lens aperture [41].

Modern digital video cameras can resolve $> 10^6$ pixels at a rate of 24 Hz . Instead of capturing images at a rate of 24 frames/sec, a digital video camera could be used as a line-of-sight wireless communication receiver. The transmitter array would be composed of LEDs with a range dependent spacing selected to ensure that the camera focused individual transmitter elements on distinct detector elements.

This hypothetical system demonstrates the principle of line-of-sight spatial multiplexing. A practical system would require fewer parallel channels with higher channel data rates.

2.3 Line-of-Sight Wireless Link

This section presents an analysis of millimeter-wave line-of-sight links employing spatial multiplexing. Section 2.3.1 analyzes the proposed system using the principles of diffraction limited optics. Section 2.3.2 explores signal propagation and channel recovery. The system is characterized as a minimally populated, multiple beam phased array in Section 2.3.3. Section 2.3.4 examines the grating lobe pattern created by the multiple element receiver.

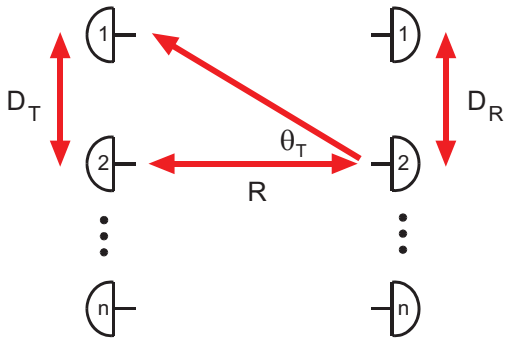

Figure 2.4: Line-of-Sight Link geometry

2.3.1 Spatial Multiplexing

LOS spatial multiplexing [42] exploits the principles of diffraction-limited optics. The transmitter and receiver use either 1 × n linear or n × n rectangular antenna arrays whose elements are separated by distances D_T and D_R (Figure 2.4), selected to ensure the angular separation of the transmitter elements is greater than or equal to the angular resolution of the receiver array:

$$\theta_T \cong \frac{D_T}{R} \tag{2.2}$$

$$\theta_{res} \cong \frac{\lambda}{n \cdot D_R} \tag{2.3}$$

$$\theta_T \geq \theta_{res} \tag{2.4}$$

where θ_T is the angular separation of the transmitter elements, θ_{res} is the angular resolution of the receiver array, R is the link range, and λ is the carrier wavelength

[36]. (2.4) leads to the relationship

$$D_R \cdot D_T = R \cdot \lambda / n. \tag{2.5}$$

(2.5) is also known as the Rayleigh Criterion which describes the diffraction-limited resolution of an optical system [41].

For line-of-sight links using linear arrays of a fixed total length, the maximum number of spatially multiplexed channels varies as the inverse of carrier wavelength (2.4). For rectangular arrays, the maximum number of channels varies as $1/\lambda^2$. If the dimensions of the transmitter and receiver are fixed, then a significant advantage in spatial multiplexing gain is obtained by operating at higher carrier frequencies. Millimeter-wave operation is particular attractive given the large available bandwidths.

2.3.2 Signal Propagation and Channel Recovery

LOS spatially multiplexed links can be analyzed by calculating the relative phase shifts experienced by the signal vectors as they propagate between the antenna arrays. Figure 2.5 represents transmitted and received signals as vectors in the I/Q plane.

The system is characterized by a channel matrix H whose (normalized) elements $h_{m,n}$ correspond to the complex channel gain from the n^{th} transmitter element to the m^{th} receiver element.

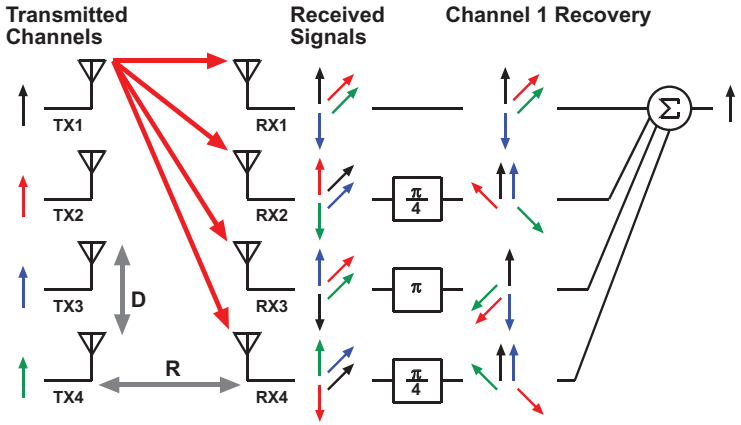

Figure 2.5: Signal propagation and channel recovery example for an ideal four-channel line-of-sight spatially multiplexed link

If channel losses are equal, then

$$h_{m,n} = e^{-i\frac{2\pi}{\lambda}(d(m,n)-R)}, \tag{2.6}$$

where *d(m,n)* is the distance between the n^{th} transmitter and the m^{th} receiver elements [36]. Inverting this channel matrix and applying it to the array of received signals separates the individual channels (Figure 2.5).

2.3.3 Multiple Beam Phased Array

The receiver array can be characterized as a minimally populated, multiple beam phased array paired with an identical transmitter array ($D_T = D_R$). The receiver has the minimum number of antennas required to steer a beam at an arbitrary transmitter element and place nulls in the directions of the other trans-

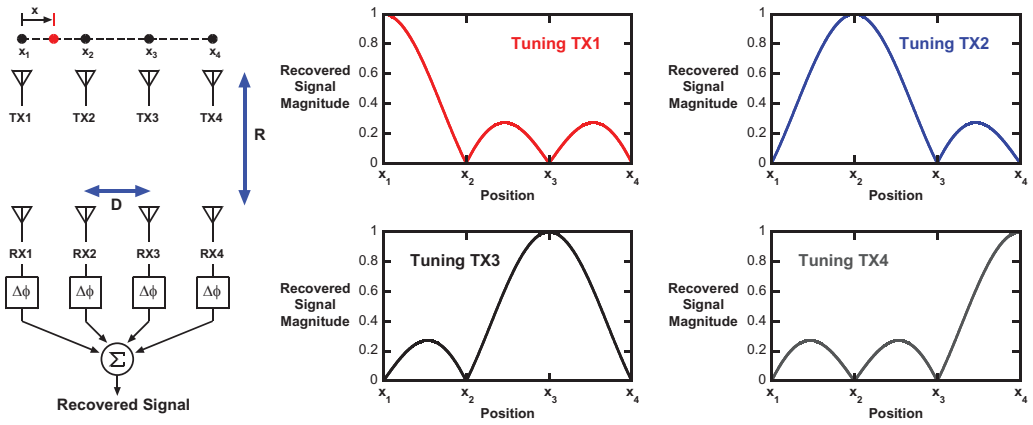

Figure 2.6: Multiple beam phased array

mitters (Figure 2.6). The plots on the right of Figure 2.6 show the recovered signal magnitude as a function of of the position of a point source x moving on a line connecting the transmitter array elements. Simultaneously focusing the receiver array at each transmitter element does not require additional antenna array elements; only additional channel separation hardware is needed to separate multiple transmitter signals.

2.3.4 Receiver Array Grating Lobes

Figure 2.7 plots the normalized antenna patterns of both a conventional single element LOS link and a four-element link using spatial multiplexing. The patterns were calculated by moving a point source on a line connecting the transmitter array at a distance of 1 km from the receiver array. Both links use 44 dB_i parabolic

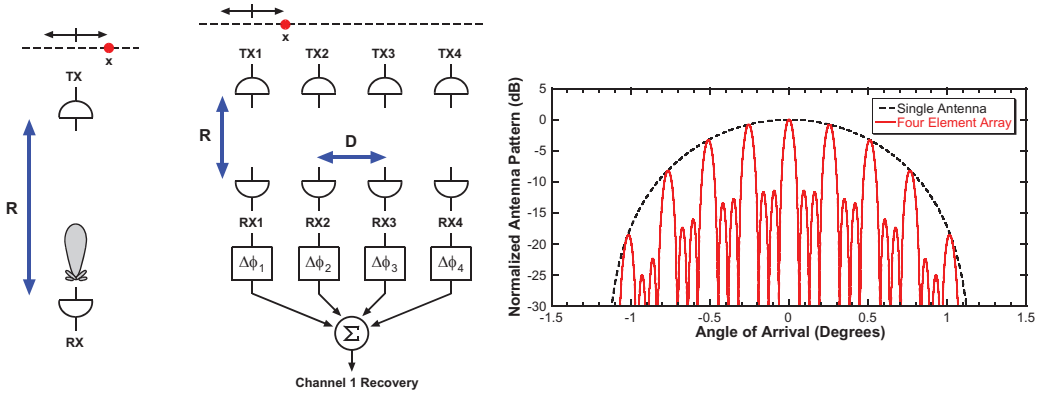

Figure 2.7: Normalized antenna patterns for single element line-of-sight link and a four element linear array using spatial multiplexing

dish antennas and a 60 GHz carrier. The phase shifts applied to the received signals of the four element link were selected to aim the receiver array at transmitter 1 and place nulls in the directions of the other transmitter elements.

The four element link response has several grating lobes corresponding to the periodic response of the receiver array. The main beam is followed by three nulls corresponding to the angle of arrival of signals from the other transmitters in the array. This pattern is repeated as the point source moves to either the left or right of the transmitter array elements. It should be noted that these receiver grating lobes do not fall on the actual transmitter array; they are simply locations where the system is most susceptible to interferers.

The grating lobe peaks are limited by the narrow beam of each parabolic dish antenna element (Figure 2.7). The four element link is therefore *less* susceptible

to a randomly placed interferer than a conventional single element point-to-point link. The presence of grating lobes between adjacent transmitter array elements indicates the link may be susceptible to errors in antenna placement.

2.4 Link Sensitivity

The performance of line-of-sight links is sensitive to antenna positioning and array alignment errors, multipath signal propagation, and atmospheric refraction. This section will examine the effect of these phenomenon on line-of-sight wireless links employing spatial multiplexing.

2.4.1 Antenna Position and Alignment Errors

This section considers the effect of errors in antenna positioning on link performance. Deviation from ideal antenna array geometry could be caused by manufacturing or installation errors or the need to use prefabricated arrays at ranges or link geometries that deviate from the design parameters.

Figure 2.8 is a diagram of the system geometry. A link may suffer from X or Y translation, range error (Z translation), array tilt (X-Z or Y-Z plane), or a rotation error (X-Y Plane).

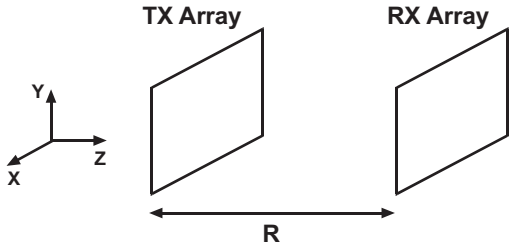

Figure 2.8: Link geometry

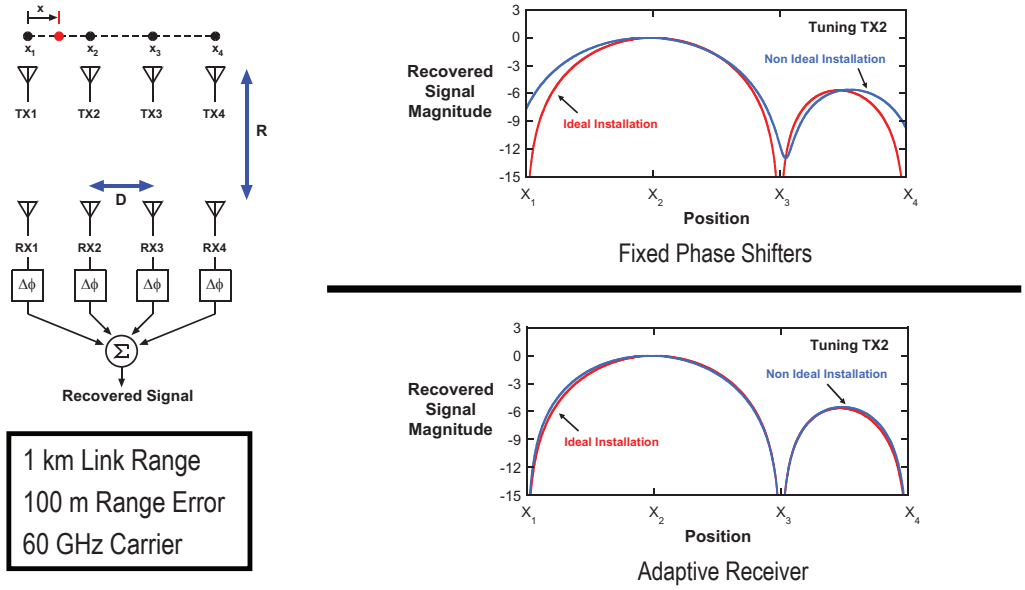

Figure 2.9: Performance of line-of-sight links in the presence of non ideal link geometry

	90% Optimal Channel Capacity
X or Y Translation	± 530 m
Range (Z Translation)	840 m to 1300 m
Tilt Error (X-Z or Y-Z Plane)	±48°
Rotation Error (X-Y Plane)	±30°

4 × 4 Rectangular Array, 1km Link Range, 20dB SNR [37]

Table 2.1: Link sensitivity to non ideal system geometry

The effects of non ideal system geometries can be minimized if the system is adaptive. Figure 2.9 plots the recovered signal magnitude for a four element array operating at a 1 km link range with a 60 GHz carrier. Two cases are considered: an array with fixed phase shifts and an adaptive receiver. The red curve plots the response of an ideal system and the blue curves plot the response of the system with a range error of 100 m. The adaptive receiver is able to steer nulls at the locations of the interfering transmitters, even under non ideal conditions. The link operating with fixed phase shifts is unable to place nulls at the proper locations and will suffer reduced performance. Channel separation for non ideal link geometries is performed by inverting the channel matrix (2.6) and applying it to the received signals

$$y = H_e \cdot x + n \tag{2.7}$$

$$H_e^{-1} \cdot y = x + H_e^{-1} \cdot n \tag{2.8}$$

where H_e is the non ideal channel matrix, y are the received signals, x are the transmitted signals, and n is the additive white Gaussian noise. The term $H_e^{-1} \cdot n$ leads to noise enhancement for non ideal link geometries and ultimately limits the link performance [37].

A detailed analysis is presented in [37]. The results for a 4×4 link operating over a 1 km link range with 2 0dB SNR are summarized in Table 2.1. The link is capable of achieving 90% of the optimal channel capacity over a wide range of antenna array positioning errors. Additional studies have also concluded that LOS links with linear and rectangular arrays are robust to small deviations in individual antenna alignment and array positioning [32–37].

2.4.2 Multipath Signal Propagation

Multipath signal propagation causes frequency dependent gain and phase variations over the channel passband of a wireless link [43]. For an outdoor line-of-sight link, ground reflections can generate a strong time delayed copy of the transmitter signal (Figure 2.10).

However, if the height of the transmitter and receiver arrays are properly selected, the effect of ground reflections can be minimized. θ_{bounce}, the incident angle of the ground reflection, is given by

$$\tan(\theta_{bounce}) \cong \theta_{bounce} \cong \frac{2 \cdot H}{R}, \tag{2.9}$$

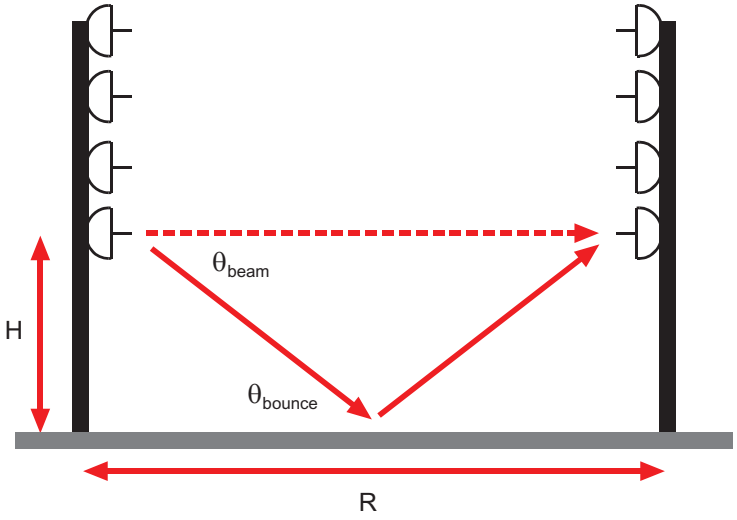

Figure 2.10: Ground reflection in an outdoor link

where H is the height of the transmitter and receiver arrays. θ_{beam}, the beam angle of the ground reflection signal, is equal to θ_{bounce}.

If the outdoor link uses a 44 dB_i parabolic dish (Section 2.3.4), a beam angle of 1^o corresponds to a 17 dB rolloff from the center of the main beam pattern (Figure 2.7). A ground reflection signal with $\theta_{bounce} > 1^o$ would have a received signal magnitude more than 30 dB below the line-of-sight signal at the receiver. Using this relationship,

$$H > \frac{\pi \cdot R}{360}. \tag{2.10}$$

For a 1 km link, H must be greater than 9 m to avoid a significant ground reflection. This roughly corresponds to the height of a three story building. In an urban environment, H must be increased to avoid time varying reflections from

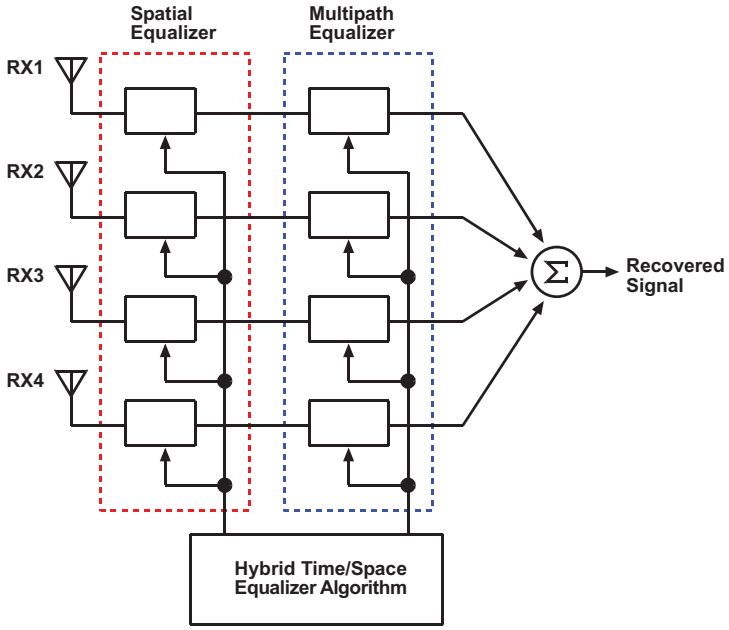

Figure 2.11: Spatial and multipath equalization

trucks or other ground level traffic. Multipath signal propagation is unavoidable for practical indoor link scenarios. Figure 2.11 is a diagram of a receiver implementing both spatial and multipath equalization. Both types of equalization must be implemented on each received signal in order to recover a single channel. The spatial and multipath equalizer hardware could be merged to form a hybrid space/time equalizer.

2.4.3 Atmospheric Refraction

Variations in atmospheric conditions (temperature, pressure, humidity, etc.) will create a non-uniform index of refraction between the transmitter and receiver arrays [44]. If an index of refraction gradient exists in the direction of signal propagation, transmitter beams will deviate from their desired trajectory.

If the transmitter beam deflection angle is larger than a receiver antenna half-power beam-width, received signal power will be greatly reduced. A single element point-to-point link will suffer a similar loss in received signal strength. Arrays composed of beam steering ICs [17–22] could be used to compensate for the atmospheric refraction of transmitter array beams.

Atmospheric scintillations create time varying amplitude and phase variations in signals arriving at the receiver [45]. The channel separation network control loop described in Chapter 5 can compensate for these effects if its time constant is sufficiently smaller than the atmospheric scintillation time constant.

2.5 Conclusions

This chapter presented an analysis of line-of-sight links employing spatial multiplexing. The basic system theory was presented and the parallels between optical imaging and line-of-sight links using spatial multiplexing were discussed.

Link sensitivity to non ideal system geometry, multipath signal propagation, and atmospheric refraction was analyzed.

Chapter 3

Channel Separation Network Design and Implementation

The channel separation network is the key system component that determines the performance of line-of-sight links employing spatial multiplexing. This chapter examines the design and performance characteristics of potential channel separation network implementations.

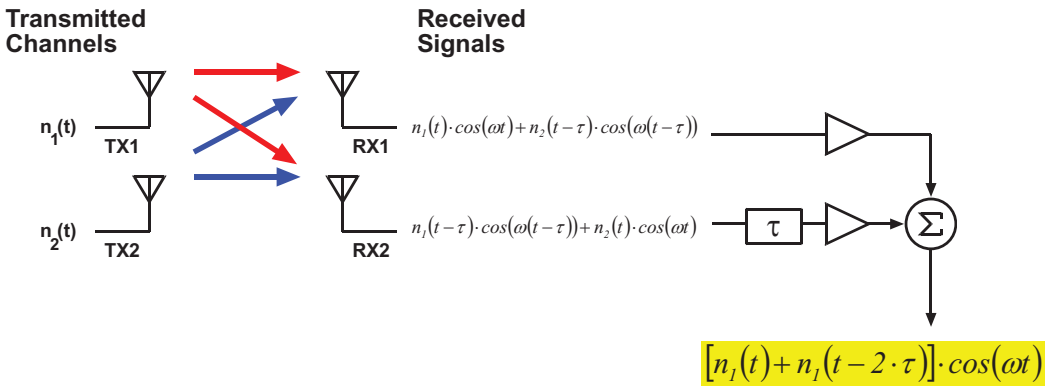

Figure 3.1: Two element time delay channel separation

3.1 Time Delay Based Channel Separation Network

MM-wave line-of-sight links employing spatial multiplexing rely on the relative time delays experienced by signals propagating from each transmitter element to the receiver array (Chapter 2). Time delay networks can be used to separate channels at the receiver.

A two element link (Figure 3.1) is the simplest example of a spatially multiplexed line-of-sight link. If $n_1(t)$ and $n_2(t)$ are the signals transmitted by transmitters 1 and 2, respectively, and ω is the carrier frequency,

$$RX_1(t + \Delta t) = n_1(t) \cdot \cos(\omega t) + n_2(t - \tau) \cdot \cos(\omega(t - \tau)) \tag{3.1}$$

$$RX_2(t + \Delta t) = n_1(t - \tau) \cdot \cos(\omega(t - \tau)) + n_2(t) \cdot \cos(\omega t) \tag{3.2}$$

then $RX_1(t)$ and $RX_2(t)$ are the signals collected by receivers 1 and 2, respectively. Δt is the delay from a transmitter to the receiver directly opposite. $\Delta t + \tau$ is the delay between a transmitter and an oblique receiver element.

Channel one can be separated from channel two:

$$n_{1recovered}(t+\Delta t) = RX_1(t+\Delta t) - RX_2(t+\Delta t-\tau) = [n_1(t)+n_1(t-2\cdot\tau)]\cdot\cos(\omega t). \tag{3.3}$$

The interfering channel is suppressed, however the channel separation network has added intersymbol interference to the recovered signal. A filter could be used to remove the intersymbol interference. The equalizer may be difficult to implement in discrete time because the time delay involved is a fraction of the carrier period and the bit period is approximately an order of magnitude larger than the carrier period. For the two channel case, the intersymbol interference is expected to be negligible (3.3).

Spatially multiplexed links can be described using a channel matrix. For a 1 $\times$ 4 linear array, the channel matrix is given by

$$H(j\omega) = \begin{bmatrix} 1 & e^{j\omega\tau} & e^{j\omega 4\tau} & e^{j\omega 9\tau} \\ e^{j\omega\tau} & 1 & e^{j\omega\tau} & e^{j\omega 4\tau} \\ e^{j\omega 4\tau} & e^{j\omega\tau} & 1 & e^{j\omega\tau} \\ e^{j\omega 9\tau} & e^{j\omega 4\tau} & e^{j\omega\tau} & 1 \end{bmatrix}. \tag{3.4}$$

The time delay network required to separate channels at the receiver is the inverse of this matrix. The channel separation matrix can be split into columns that describe the network required to separate each channel

$$H^{-1}_{channel1}(j\omega) = \beta \cdot \begin{bmatrix} 1 - 2 \cdot e^{j\omega 2\tau} + 2 \cdot e^{j\omega 6\tau} - e^{j\omega 8\tau} \\ -e^{j\omega\tau} + e^{j\omega 3\tau} + e^{j\omega 5\tau} - e^{j\omega 9\tau} - e^{j\omega 11\tau} + e^{j\omega 13\tau} \\ e^{j\omega 2\tau} - e^{j\omega 4\tau} - e^{j\omega 6\tau} + e^{j\omega 10\tau} + e^{j\omega 12\tau} - e^{j\omega 14\tau} \\ -e^{j\omega 3\tau} + 2 \cdot e^{j\omega 5\tau} - 2 \cdot e^{j\omega 9\tau} + e^{j\omega 11\tau} \end{bmatrix} \tag{3.5}$$

$$H^{-1}_{channel2}(j\omega) = \beta \cdot \begin{bmatrix} -e^{j\omega\tau} + e^{j\omega 3\tau} + e^{j\omega 5\tau} - e^{j\omega 9\tau} - e^{j\omega 11\tau} + e^{j\omega 13\tau} \\ 1 - e^{j\omega 2\tau} - e^{j\omega 8\tau} + 2 \cdot e^{j\omega 14\tau} - e^{j\omega 18\tau} \\ -e^{j\omega\tau} + 2 \cdot e^{j\omega 5\tau} - e^{j\omega 11\tau} - e^{j\omega 17\tau} + e^{j\omega 19\tau} \\ e^{j\omega 2\tau} - e^{j\omega 4\tau} - e^{j\omega 6\tau} + e^{j\omega 10\tau} + e^{j\omega 12\tau} - e^{j\omega 14\tau} \end{bmatrix} \tag{3.6}$$

$$H^{-1}_{channel3}(j\omega) = \beta \cdot \begin{bmatrix} e^{j\omega 2\tau} - e^{j\omega 4\tau} - e^{j\omega 6\tau} + e^{j\omega 10\tau} + e^{j\omega 12\tau} - e^{j\omega 14\tau} \\ -e^{j\omega\tau} + 2 \cdot e^{j\omega 5\tau} - e^{j\omega 11\tau} - e^{j\omega 17\tau} + e^{j\omega 19\tau} \\ 1 - e^{j\omega 2\tau} - e^{j\omega 8\tau} + 2 \cdot e^{j\omega 14\tau} - e^{j\omega 18\tau} \\ -e^{j\omega\tau} + e^{j\omega 3\tau} + e^{j\omega 5\tau} - e^{j\omega 9\tau} - e^{j\omega 11\tau} + e^{j\omega 13\tau} \end{bmatrix} \tag{3.7}$$

$$H^{-1}_{channel4}(j\omega) = \beta \cdot \begin{bmatrix} -e^{j\omega 3\tau} + 2 \cdot e^{j\omega 5\tau} - 2 \cdot e^{j\omega 9\tau} + e^{j\omega 11\tau} \\ e^{j\omega 2\tau} - e^{j\omega 4\tau} - e^{j\omega 6\tau} + e^{j\omega 10\tau} + e^{j\omega 12\tau} - e^{j\omega 14\tau} \\ -e^{j\omega\tau} + e^{j\omega 3\tau} + e^{j\omega 5\tau} - e^{j\omega 9\tau} - e^{j\omega 11\tau} + e^{j\omega 13\tau} \\ 1 - 2 \cdot e^{j\omega 2\tau} + 2 \cdot e^{j\omega 6\tau} - e^{j\omega 8\tau} \end{bmatrix} \tag{3.8}$$

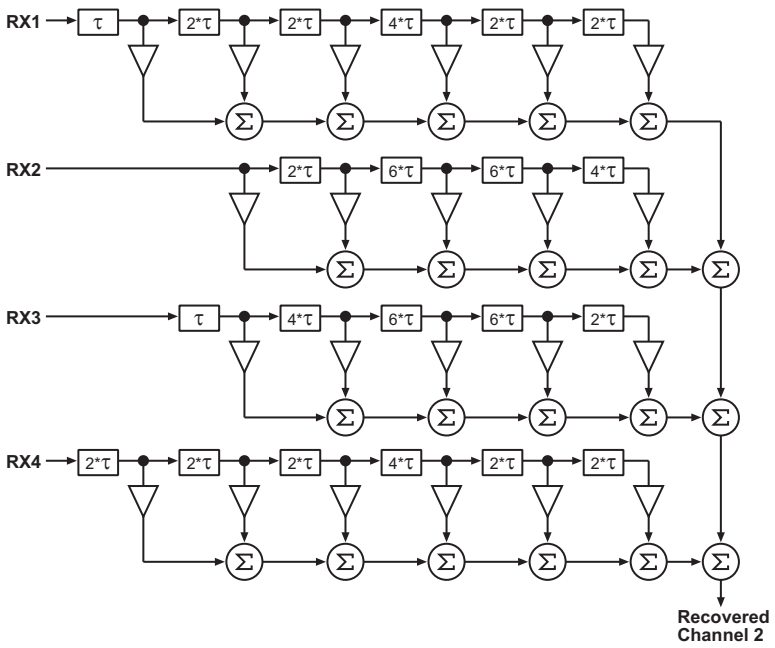

Figure 3.2: Four element time delay channel separation network for recovering channel 2

$$\beta = \frac{1}{1 - 3 \cdot e^{j\omega 2\tau} + e^{j\omega 4\tau} + 4 \cdot e^{j\omega 6\tau} - 2 \cdot e^{j\omega 8\tau} - 2 \cdot e^{j\omega 10\tau} - 2 \cdot e^{j\omega 12\tau} + 4 \cdot e^{j\omega 14\tau} + e^{j\omega 16\tau} - 3 \cdot e^{j\omega 18\tau} + e^{j\omega 20\tau}}. \tag{3.9}$$

Figure 3.2 is a diagram of the time delay network required to recover channel two (3.6). Figure 3.3 plots the time delay channel separation network complexity for linear arrays with 2-9 elements. Network complexity scales poorly for $N > 2$. The plot considers channel separation networks operating at the carrier or an IF frequency. Baseband networks suffer a factor of 4 increase in complexity.

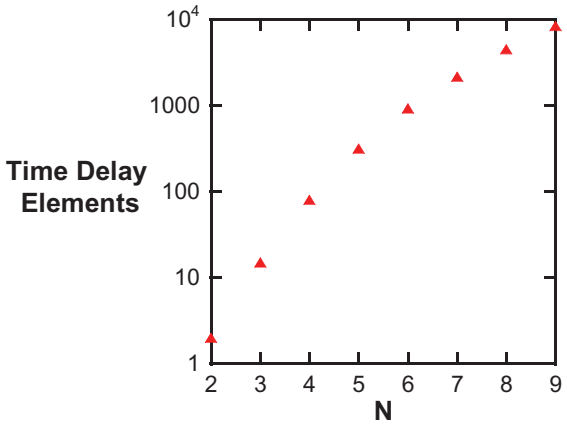

Figure 3.3: Ideal time delay channel separation nework complexity for linear arrays with N elements

3.2 Phase Shift Based Channel Separation Network

LOS links using spatial multiplexing rely on time delay variations between individual transmitter signals arriving at the receiver array elements to separate channels (Chapter 2). Ideal wideband channel separation requires variable time delay elements at the receiver to compensate for antenna positioning errors at the transmitter and receiver arrays (Section 2.4.1).

Variable time delay elements can be difficult to implement using integrated circuit technology. Phase shift elements can be easily implemented using baseband circuits in either digital or analog form. Figure 3.4 compares the complexity of ideal time delay channel separation networks to simple phase shift channel sep-

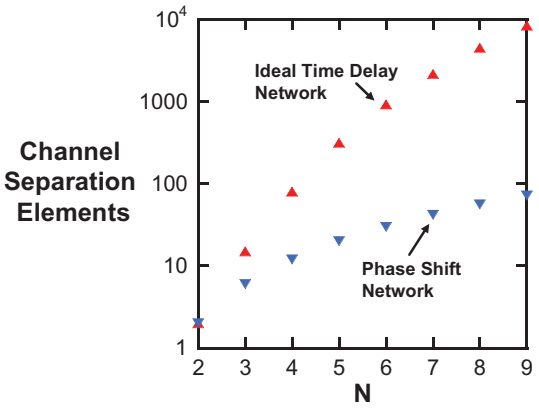

Figure 3.4: Ideal time delay and phase shift channel separation network complexity for linear arrays

aration networks for linear arrays of length N. For $N > 2$, phase shift channel separation networks are smaller than ideal time delay networks. The plot considers channel separation networks operating at the carrier frequency or at IF. Baseband channel separation networks for both cases suffer a factor of 4 increase in complexity.

This section examines the performance of phase shift based baseband channel separation networks.

3.2.1 Wideband Signal-to-Interference Ratio Performance

Over a narrow bandwidth, a time delay can be approximated as a phase shift. As signal bandwidth increases, this approximation breaks down. For a spatially multiplexed link, this leads to a decrease in signal-to-interference ratio (SIR) at the

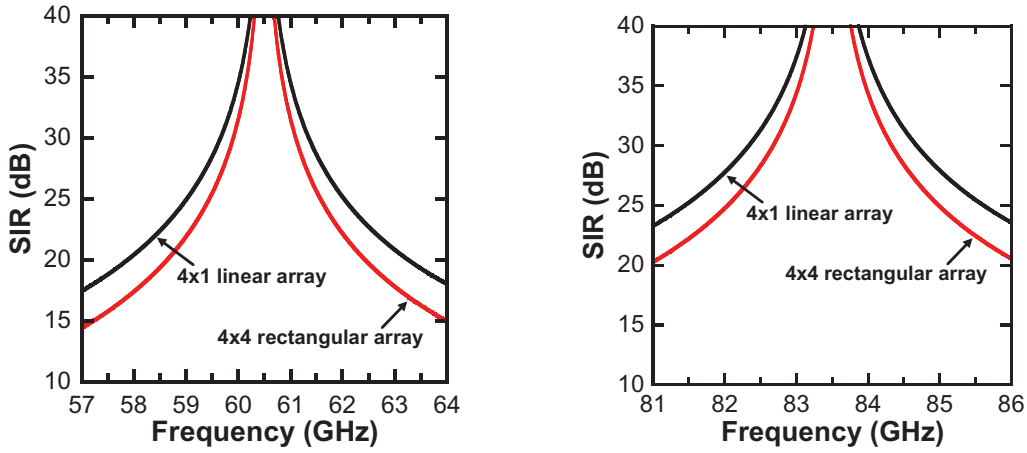

(a) 60.5 GHz carrier

(b) 83.5 GHz carrier

Figure 3.5: SIR as a function of frequency for 60 and 80 GHz links using phase shift channel separation networks

edges of the signal passband. However, phase shift channel separation networks can be implemented with simple baseband circuits, whereas variable-delay circuits are more complex and difficult to realize over wide signal bandwidths. A pair of four-quadrant analog multipliers operating on the I and Q components of a baseband signal can perform arbitrary magnitude and phase shift operations.

Figure 3.5 plots the single tone SIR response of 1×4 linear and 4×4 rectangular antenna arrays operating at 57-64 GHz and 81-86 GHz over a 1 km range. The carrier frequency is placed at the center of the passband. These plots represent the worst case performance of an ideal system, which occurs when the receiver array is aimed at an inner transmitter array element.

3.2.2 Effect of Residual Interference Power on Bit Error Rate

Recovered signal bit error rates (BER) can be related to receiver SIR after channel separation. If we ignore the frequency dependence of the SIR, the BER is readily calculated as a function of E_b/N_o and the SIR for a system with an arbitrary number of channels. E_b is the energy per bit and $N_o/2$ is the variance of additive gaussian noise.

The resulting expression provides a general understanding of BER performance in the presence of limited SIR. If a system has *M=n-1* interferers of equal power and uses BPSK signaling, then

$$y(t) = s(t) + \alpha \sum_{i=1}^{M} x_i(t) + n(t), \tag{3.10}$$

where *y(t)* is the recovered signal, α^2 is the power of an individual interferer, *n(t)* is additive gaussian noise with zero mean and variance $N_o/2$, and

$$s(t) \in \left\{ -\sqrt{E_b}, +\sqrt{E_b} \right\} \tag{3.11}$$

$$x_i(t) \in \left\{ -\sqrt{E_b}, +\sqrt{E_b} \right\} \tag{3.12}$$

where *s(t)* is the desired symbol and $x_i(t)$ are interfering symbols.

Total SIR is

$$SIR = \frac{1}{\alpha^2 \cdot M}. \tag{3.13}$$

For the case of one interferer,

$$y(t) = s(t) + \alpha \cdot x_1(t) + n(t). \tag{3.14}$$

Assume, without loss of generality, *s(t)* = -1. An error occurs if *y(t)* > 0. It can be shown that the error probability is

$$P_{error} = \frac{1}{2} \cdot Q\left((1+\alpha) \cdot \sqrt{\frac{2 \cdot E_b}{N_o}}\right) + \frac{1}{2} \cdot Q\left((1-\alpha) \cdot \sqrt{\frac{2 \cdot E_b}{N_o}}\right), \tag{3.15}$$

where Q is the complementary error function. Generalizing to M interferers,

$$P_{error} = \frac{1}{2^M} \cdot \sum_{k=0}^{M} \begin{pmatrix} M \\ k \end{pmatrix} \cdot Q\left((1+\alpha \cdot (M-2 \cdot k)) \cdot \sqrt{\frac{2 \cdot E_b}{N_o}}\right), \tag{3.16}$$

where

$$\begin{pmatrix} M \\ k \end{pmatrix} = \frac{M!}{k! \cdot (M-k)!} \tag{3.17}$$

is the number of combinations of M elements taken k at a time.

Figure 3.6 plots BER versus E_b/N_o as a function of SIR for 1 × 4 linear and 4 × 4 rectangular antenna arrays using BPSK signaling. BER degradation is minimal for SIR levels above 20 dB for linear and rectangular arrays.

From Figure 3.5, the performance of ideal 80 GHz systems using phase shift based channel separation networks meet the SIR requirements for tolerable BER degradation. The 60 GHz links have SIR < 20 dB at the edges of the passband. This analysis approximates the BPSK data spectrum as tones placed at the edges

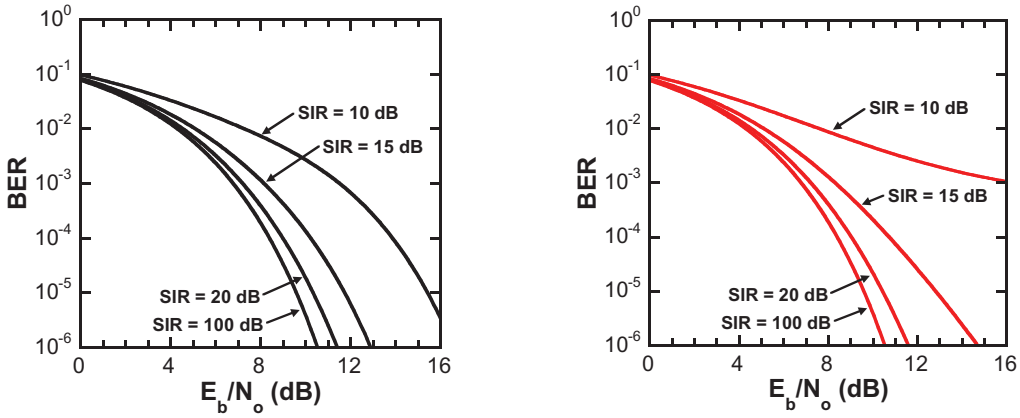

(a) 1 × 4 linear array

(b) 4 × 4 rectangular array

Figure 3.6: BER performance of 1 × 4 linear and 4 × 4 rectangular arrays as a function of SIR

of the passband and represents a lower bound on the BER performance of the system.

The analysis described in this section also applies to QPSK signals using a gray bitmap [43]. This method of analysis can be applied to other signal modulation schemes, such as DPSK and DQPSK.

3.3 Approximating Ideal Time Delay Channel Separation Network

Ideal time delay channel separation networks scale poorly for linear arrays containing more than two elements (Figure 3.3). Phase shift based channel sepa-

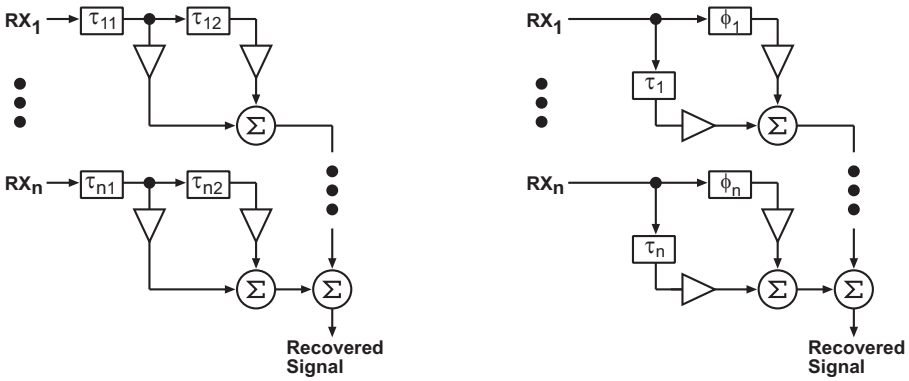

(a) Dual time delay channel separation newtwork

(b) Time delay and phase shift channel separation newtwork

Figure 3.7: Alternative channel separation networks

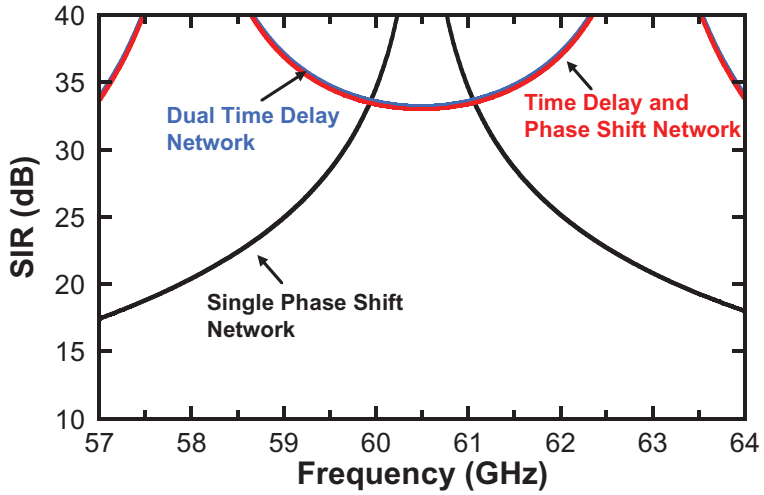

Figure 3.8: SIR performance for 1 × 4 linear array channel separation networks

ration networks reduce system complexity, however they suffer from reduced SIR performance at the edges of the signal passband (Figure 3.5).

Channel separation networks consisting of pairs of time delays (Figure 3.7(a)) or a time delay and and a phase shift element (Figure 3.7(b)) could be used to approximate the ideal time delay channel separation network over a broader bandwidth than single phase shift based channel separation networks. Each element of a dual time delay channel separation network is given by

$$H_{m,n} = \alpha_{1(m,n)} \cdot e^{j\omega \cdot n_{1(m,n)} \cdot \tau} + \alpha_{2(m,n)} \cdot e^{j\omega \cdot n_{2(m,n)} \cdot \tau}, \tag{3.18}$$

where $\alpha_{1(m,n)}$, $\alpha_{2(m,n)}$, $n_{1(m,n)}$, and $n_{2(m,n)}$ are gain and time delay parameters used to approximate the phase and magnitude response of the ideal time delay channel separation network.

A time delay/phase shift channel separation network has a transfer function given by

$$H_{m,n} = \alpha_{1(m,n)} \cdot e^{j\omega \cdot n_{1(m,n)} \cdot \tau} + \alpha_{2(m,n)} \cdot e^{j \cdot \phi_{2(m,n)}}, \tag{3.19}$$

where $\phi_{2(m,n)}$ is a phase shift parameter used to approximate the phase and magnitude response of the ideal time delay channel separation network.

These networks can be used to approximate the ideal time delay channel separation network. Both networks are capable of exactly matching the performance of an ideal channel separation network at two frequencies. Other methods can be

used to design the networks to approximate the magnitude and phase response over a given bandwidth [46].

Figure 3.8 plots the wideband SIR performance of single phase shift, dual time delay, and time delay/phase shift channel separation networks for a 1×4 linear array operating at 60 GHz. The two element channel separation networks have nearly the same SIR performance. The channel separation networks were designed to match the performance of the ideal time delay channel separation network at two frequencies: 58 and 63 GHz. Other methods for approximating the ideal time delay channel separation network could be used to shape the SIR performance as a function of frequency.

SIR is > 30 dB over the entire signal band. This ensures that residual cross channel interference will have very little effect on system performance. SIR $>$ 20 dB has little effect on BER as a function of E_b/N_o (Figure 3.6). These results demonstrate that channel separation network complexity can be traded for improved wideband SIR performance.

3.4 Channel Separation Network Placement

The receiver channel separation network for a wireless link employing spatial multiplexing could be placed at three different frequencies: mm-wave carrier, IF,

or at baseband. Receiver signal distribution is a major disadvantage for channel separation networks operating at the system carrier frequency. Cables capable of carrying mm-wave frequencies are expensive and lossy, given receiver element separation on the order of 1 m for a link range on the order of 1 km (Chapter 2). Further, a mm-wave channel separation network eliminates the possibility of digital channel separation and requires complex analog circuitry operating at mm-wave frequencies.

Operation at IF frequency easies the problem of receiver signal distribution. The carrier frequency must remain above 2 GHz, given the wide bandwidths available at mm-wave carrier frequencies. IF operation increases the size of the analog channel separation network compared to mm-wave operation. Tuned circuits require bulky on chip reactive elements.

Baseband channel separation networks have several advantages. Direct down-conversion receivers can be used, reducing receiver IC complexity. Baseband signal distribution allows the use of cheaper cables, however the baseband signals will have bandwidths of 5 -7 GHz, requiring the use of high quality coaxial cables.

Analog circuit based channel separation networks do not require bulky tuning networks, reducing the die area requirements. Baseband operation also allows the possibility of a DSP based channel separation network.

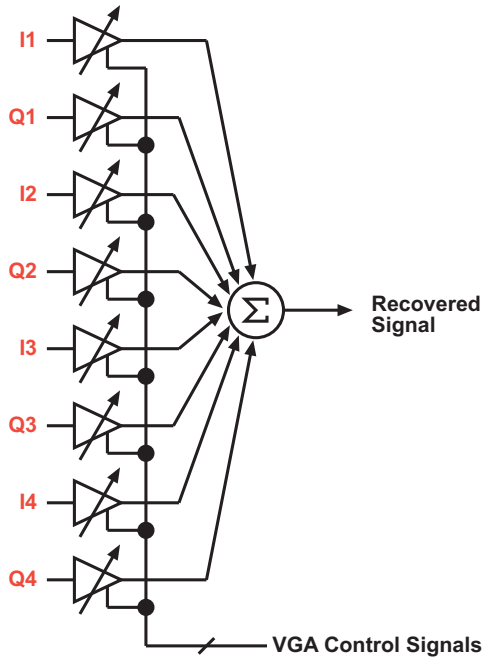

Figure 3.9: Analog channel recovery

3.5 Baseband Channel Separation Network Implementations

Baseband channel separation networks offer several advantages over RF or IF channel separation networks (Section 3.4). Phase shift based channel separation networks offer reasonable performance and straight forward implementation using either analog or digital circuits.

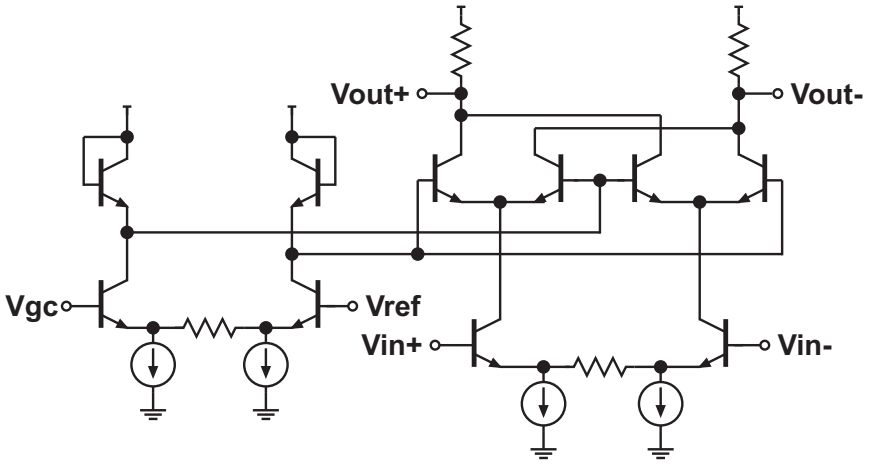

Figure 3.10: Custom IC four quadrant analog multiplier

3.5.1 Analog Channel Separation Network

The phase shift based channel separation network described in Section 3.2 can be implemented with simple analog circuits (Figure 3.9). Four quadrant analog multipliers implement arbitrary vector operations (phase shift and magnitude scaling) by operating on the complex baseband signals from each receiver. The four quadrant analog multiplier can be implemented using bipolar transistors (Figure 3.10). This circuit, first proposed by Barry Gilbert, features a linear gain control curve [47].

Degenerated differential pairs provide linearized voltage to current conversion for both the input signal and the gain control signal. Diode connected loads on the gain control differential pair create an inverse hyperbolic tangent current to voltage transfer function. This nonlinearity predistorts the signal before it is

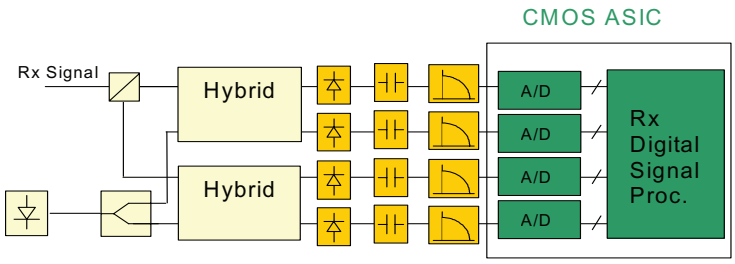

Figure 3.11: 40 Gb/s QPSK receiver [1]

applied to the bases of the upper differential pairs. The upper differential pairs have a hyperbolic tangent voltage to current transfer function. The overall gain control transfer function is linear, assuming the transistor are matched [47].

3.5.2 DSP Based Channel Separation Network

Recent work on QPSK optical links implies that digital channel separation is possible (Figure 3.11). The system uses a custom IC, implemented with 90nm CMOS, that contains four 20 GS/s ADCs capable of 6 bit resolution over a 6 GHz 3 dB bandwidth. An on chip DSP consisting of 20 million gates and capable of 12×10^{12} operations per second performs the required receiver signal processing operations, including carrier and clock recovery in addition to polarization and dispersion compensation. The IC dissipates 20 W [1].

Figure 3.12 is a block diagram of a four element receiver using digital channel separation. If the system uses QPSK signaling, a BER of 10^{-6} requires an $\frac{E_b}{N_o}$ of

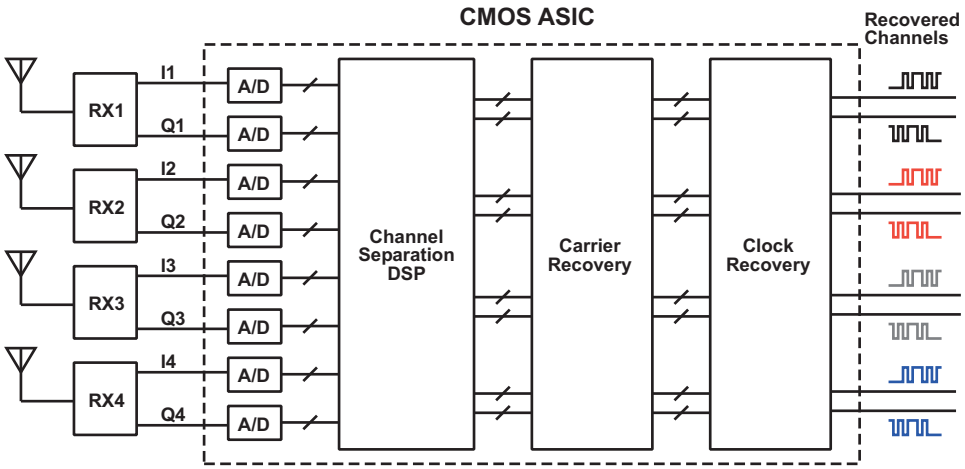

Figure 3.12: Four element, 40 Gb/s digital receiver

∼11 dB. A 15 dB system margin gives a recovered signal SNR of 26 dB. An ideal 6 bit ADC has a dynamic range of ∼36 dB, placing the quantization noise floor 10 dB below the recovered signal noise floor.

At 60 GHz, each I and Q channel is limited to 3.5 GHz bandwidth which is below the 6 GHz 3 dB bandwidth of the ADCs used in the 40 Gb/s optical link. Additional receiver functions, including carrier and clock recovery, could be implemented with digital or mixed-signal circuits.

The analog channel separation network described in Section 3.5.1 can be implemented with digital circuits (Figure 3.13). Four quadrant analog multipliers are implemented using multiply/accumulate (M/A) digital blocks. M/A blocks consist of a digital multiplier and a two input adder circuit (Figure 3.13). This circuit architecture is identical to FIR filters routinely implemented on DSPs. In-

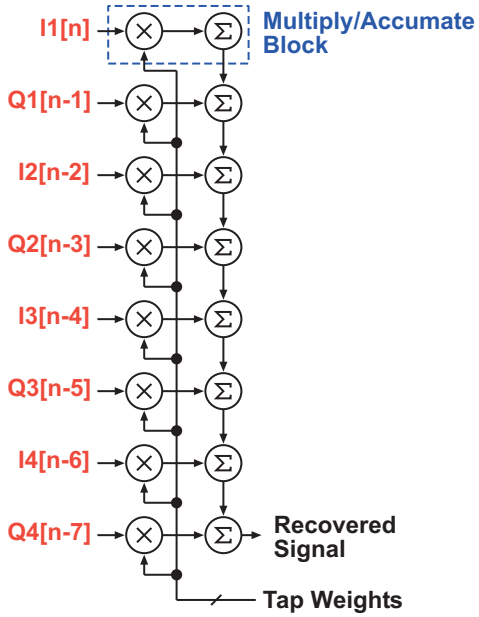

Figure 3.13: Digital channel recovery

put signals are delayed in order to compensate for the delays in signal propagation through the multiply/accumulate chain.

A digital channel separation network for a 1 × 4 linear array requires 64 M/A blocks operating at full speed. Power Consumption/Die Area tradeoffs may dictate the need for parallel operation of slower M/A blocks. The number of M/A blocks required for a given sampling rate and M/A clock speed is given by

$$M/A\ Blocks = 8 \times 8 \times \frac{sampling\ rate}{M/A\ clock\ rate}. \tag{3.20}$$

Further work is needed to determine the feasibility of an all digital or mixed signal receiver for line-of-sight links employing spatial multiplexing. Open questions

Range (m)	Frequency (GHz)	n	Array Length (m)	Data Rate[1] (Gb/s)
1000	83.5	2	1.24	29
		3	2.19	65
		4	2.84	115
100	83.5	2	0.42	29
		3	0.69	65
		4	0.90	115
10	60.5	2	0.16	40
		3	0.26	90
		4	0.33	160

[1]Assuming n $\times$ n rectangular arrays, QPSK modulation, $\alpha = 0.4$

Table 3.1: Sample Link Configurations

include power consumption and die area requirements compared to analog circuit implementations.

3.6 Sample Link Configurations

Table 3.1 provides sample link configurations illustrating potential array sizes, link ranges, and data rates. Array sizes $n = 2, 3, 4$ are considered, corresponding to 4, 9, 16 element rectangular arrays. Two outdoor link ranges (100 m and 1 km) are considered and a 10 m indoor link example is also specified. A carrier frequency of 83.5 GHz is assumed for the outdoor link examples and a 60.5 GHz carrier is used for the indoor link. Long range links are unattractive at 60 GHz due to significant signal attenuation caused by oxygen absorption.

The length of a spatially multiplexed array is given by

$$L = D \cdot (n - 1) \tag{3.21}$$

where D is the antenna element spacing given by (2.5), assuming $D_T = D_R$. The outdoor link calculation assumes a 5 GHz channel bandwidth (81-86 GHz) and the indoor link assumes a 7 GHz data bandwidth (57-64 GHz).

Data rates are provided for $n \times n$ arrays assuming a 1.4 bit/s/Hz spectral efficiency. This spectral efficiency could be achieved with QPSK modulation and an excess bandwidth factor $\alpha = 0.4$. A mm-wave link with a spectral efficiency of 2.4 bit/s/Hz has been reported [7] and higher spectral efficiencies can be expected in the future. Exploiting cross polarization diversity [29] could double the link data rates listed in Table 3.1. For example, a link using 4×4 arrays could support 230 Gb/s in the 81-86 GHz band.

Although an emphasis has been placed on outdoor links, it should be noted that large aggregate data rates can be achieved for indoor links exploiting LOS spatial multiplexing. As shown in Table 3.1, arrays for short range links scale down to sizes well suited for integration with devices such as set-top boxes, laptops, and HD displays.

3.7 Conclusions

This chapter presented an analysis of channel separation networks for line-of-sight links employing spatial multiplexing. The channel separation network is the most important component of these systems and determines system performance. Ideal time delay channel separation networks were derived. Simple phase shift networks were examined as an alternative to the ideal time delay channel separation network. Dual time delay and time delay/phase shift networks were shown to improve wideband SIR performance compared to phase shift channel separation networks at the cost of increased system complexity. Digital and analog implementations were examined and compared. Link examples were presented.

Chapter 4

Two-Element Prototype: IF Channel Separation

This chapter describes the initial two-element prototype that was built to demonstrate the feasibility of spatial multiplexing at millimeter-wave frequencies. The following section presents the system architecture. A detailed description of the hardware prototype and experimental results from both indoor and outdoor testing are presented in the remaining sections.

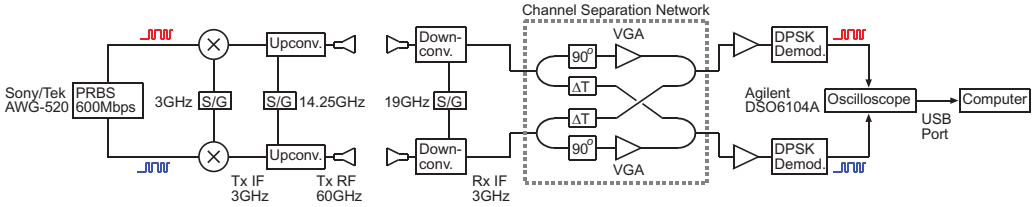

Figure 4.1: Two-channel MIMO hardware prototype block diagram

4.1 System Architecure

The initial prototype effort consisted of two-element transmitter and receiver arrays (Figure 4.1). IF channel separation was chosen to reduce system complexity and the time required to build and test the prototype. A 60 GHz carrier frequency was chosen for the wide variety of waveguide components available at V-band and the reduced FCC regulations compared to other millimeter-wave bands. The following section describes the design and construction of the transmitter and receiver hardware prototypes.

4.2 Prototype Design and Construction

The hardware prototype (Figure 4.1) was constructed from commercially available millimeter-wave and RF components and consists of a two-element transmitter and a two-element receiver. Section 4.2.1 describes the transmitter array pro-

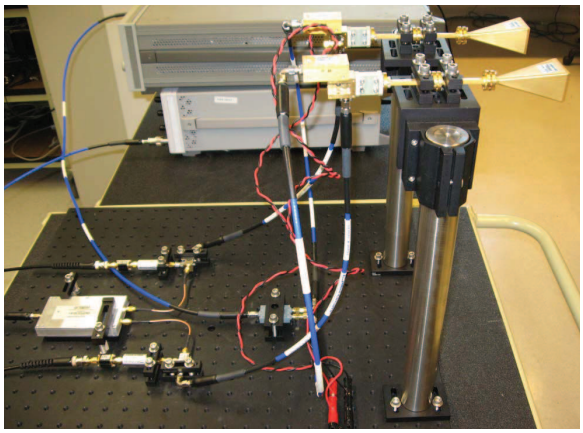

Figure 4.2: Transmitter prototype

totype. The receiver array is described in Section 4.2.2 and the receiver channel separation network is presented in Section 4.2.3.

4.2.1 Transmitter Array

The transmitter (Figure 4.1) consisted of a baseband data source, BPSK modulator, and 60 GHz upconverter stages. The baseband data source generated two independent Pseudo Random Bit Sequences (PRBS) at 600 Mb/s with sequence length $2^{17} - 1$. The PRBS data streams were generated using different maximal length shift register feedback configurations, ensuring that the two channels carry independent data. A 3 GHz IF carrier with BPSK modulation was obtained by applying these data signals, in bipolar format, to the baseband port of a mixer operating with a 3 GHz local oscillator. Using a second mixer, the 3 GHz BPSK

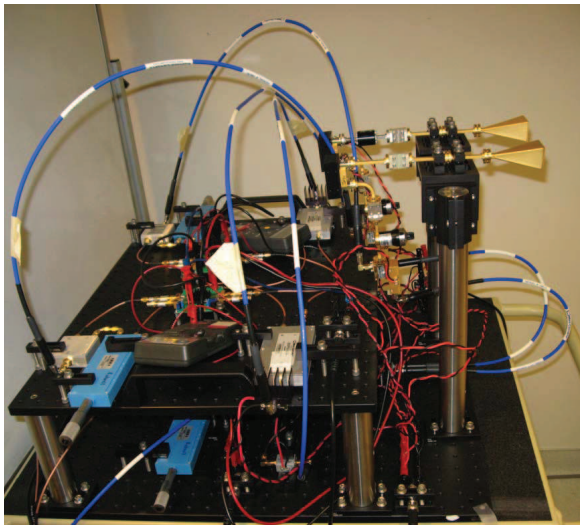

Figure 4.3: Indoor receiver prototype

signal was upconverted to 60 GHz. A 58-62 GHz bandpass filter suppressed both the mixer image response and LO feedthrough. The transmitter used 24 dB_i standard gain horn antennas for both indoor and outdoor experiments (Figure 4.2). The transmitter element spacing was increased from 12 cm for indoor testing (6 m link range) to 32 cm spacing for outdoor testing (41 m link range).

4.2.2 Receiver Array

The receiver (Figure 4.1) contained a 60 GHz downconverter, an IF channel separation network, a data demodulator, and data capture hardware. The downconverter block brought the received signals to a 3 GHz IF and contained a bandpass filter, an LNA, and a mixer.

Figure 4.4: Outdoor receiver prototype

The channel separation network was placed at the IF frequency. Nominally, this network is composed of two fixed 90^o phase shifts. To accommodate variations from the nominal case of the relative gains and phases of the four propagation paths, variable-gain and variable-delay elements were provided in the channel separation network. These elements were manually adjusted to null the cross-channel interference.

After separating the channels, data was demodulated using a Differential Phase Shift Keying (DPSK) demodulator. Carrier recovery at the receiver is not required. The demodulator operated at the 3 GHz IF and consisted of a power

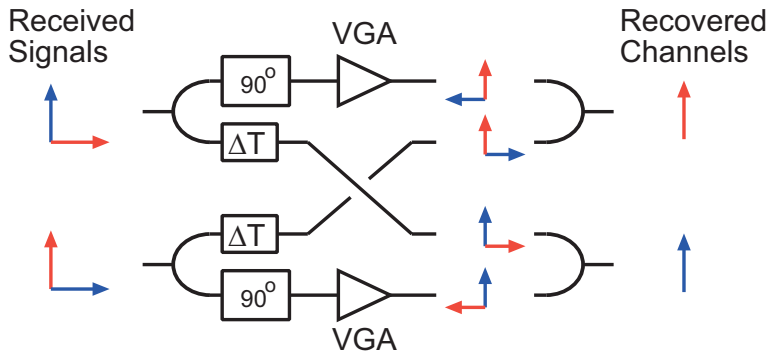

Figure 4.5: IF channel separation network

splitter, a 1-bit-period delay element, and a mixer. This allowed the demodulator to combine data demodulation and downconversion to baseband.

The recovered data was captured on a multiple channel oscilloscope controlled by a laptop computer. Both recovered channels were digitized simultaneously for subsequent bit error rate (BER) analysis. The oscilloscope memory size limited the amount of data that could be captured and prevented measurement of error rates below 10^{-6}.

The receiver prototype used 24 dB_i standard gain horn antennas at 12 cm spacing for indoor testing (Figure 4.3). For outdoor testing, the receiver was equipped with s 40 dB_i Cassegrainian antennas at 32 cm spacing (Figure 4.4).

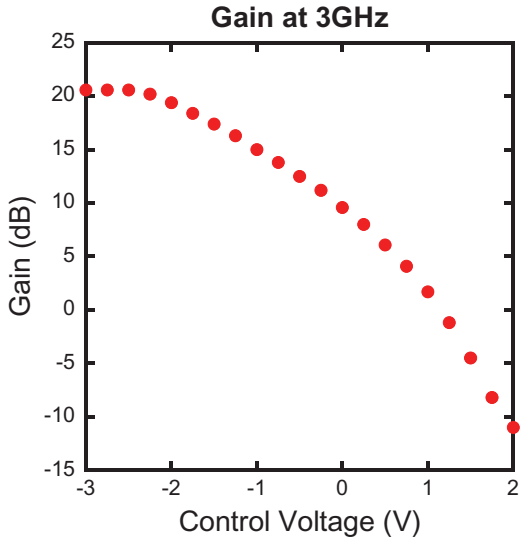

Figure 4.6: Variable-gain amplifier gain control curve

4.2.3 Receiver Channel Separation Network

The IF channel separation network (Figure 4.5) consisted of pairs of manually-tuned coaxial line stretchers and variable gain amplifiers. The variable-gain amplifiers had 3 dB bandwidths in excess of 10 GHz. Figure 4.6 is a plot of the gain of the variable-gain amplifiers as a function of control voltage.

4.3 Experimental Results

The two-element hardware prototype was tested in both an indoor office environment at a range of 6 m and outdoors at a 41 m link range. Table 5.1 summarizes the indoor experiment link budget and Table 4.2 presents the outdoor link budget.

TX Antenna Gain	24	dB_i
RX Antenna Gain	24	dB_i
RX Power	6	m
Free-Space Path Loss	84	dB
RX Noise Figure	8	dB
BER	10^{-6}	
Link Margin	13	dB
TX Power	-17	dBm
RX Power	-53	dBm

Table 4.1: Indoor Link Budget

TX Antenna Gain	24	dB_i
RX Antenna Gain	40	dB_i
RX Power	41	m
Free-Space Path Loss	100	dB
Atmospheric Attenuation	1	dB
RX Noise Figure	8	dB
BER	10^{-6}	
Link Margin	13	dB
TX Power	-17	dBm
RX Power	-54	dBm

Table 4.2: Outdoor Link Budget

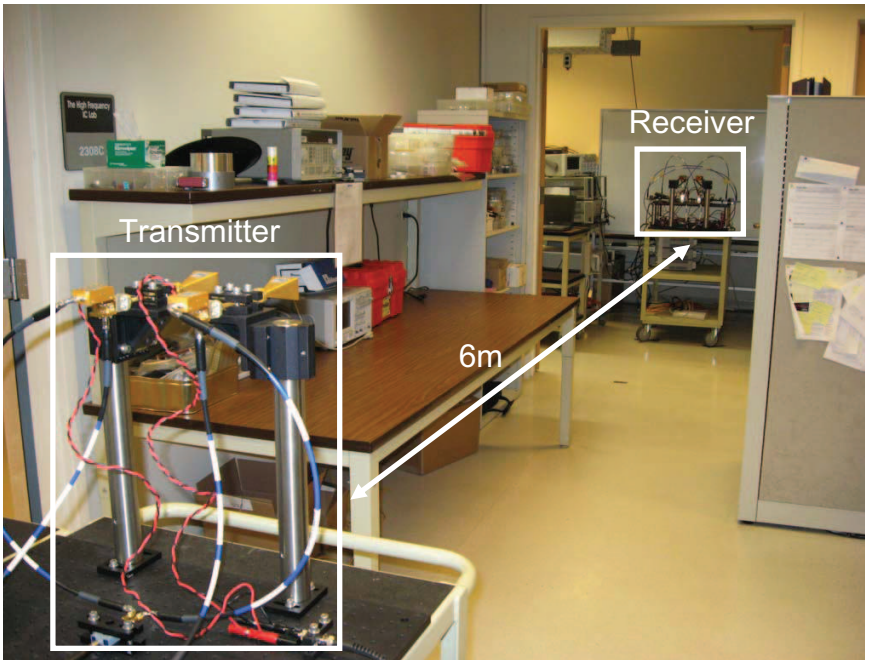

Figure 4.7: Indoor radio link experiment

Results from the indoor and outdoor experiments are presented and analyzed in the following sections.

4.3.1 Indoor Results

The hardware prototype was tested in an indoor office environment at a range of 6 m (Figure 4.7). The transmitter and receiver antenna pairs were separated by 12.4 cm. Horn antennas were used in the transmitter and receiver arrays. The receiver channel separation network was tuned by operating the PRBS source at 10 Mb/s. The spectrum of each output of the channel separation network was

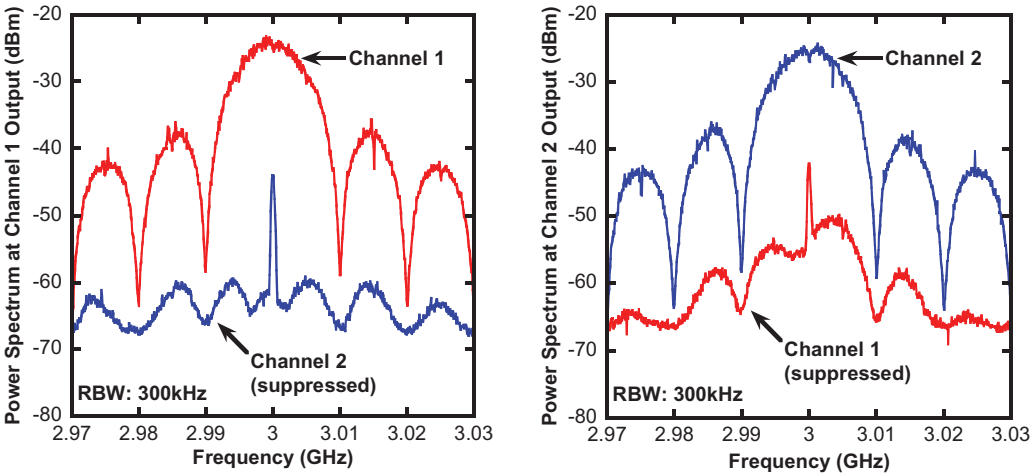

Figure 4.8: Indoor channel separation network performance at 10 Mb/s

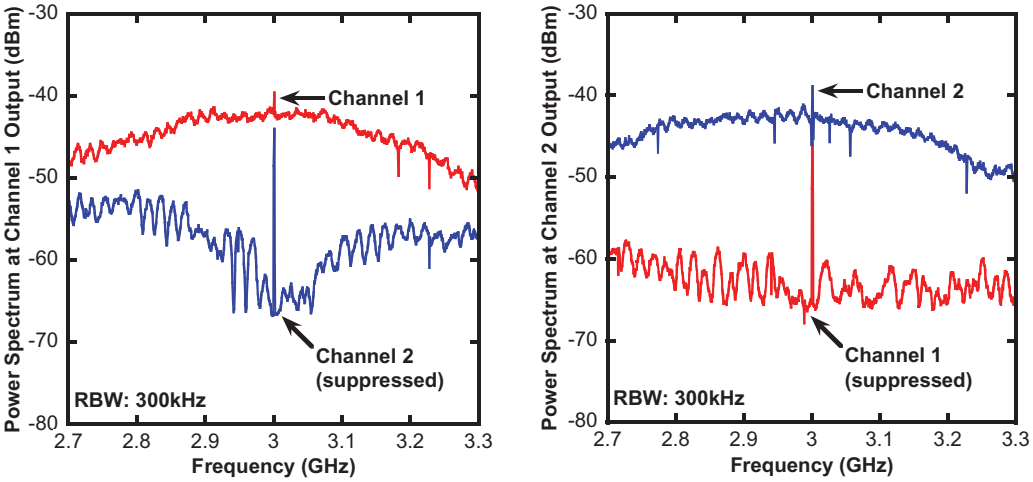

Figure 4.9: Indoor channel separation network performance at 600 Mb/s

	Channel Number	1	2
BER	Single Active Transmitter	$< 10^{-6}$	$< 10^{-6}$
	Two Active Transmitters	$< 10^{-6}$	$< 10^{-6}$
Signal-to-Interference Ratio	10 Mb/s per channel	29 dB	24 dB
	600 Mb/s per channel	12 dB	18 dB

Table 4.3: Summary of indoor measurements

observed on a spectrum analyzer. Gain and time shift elements were iteratively tuned to minimize the undesired transmitter signals. Figure 4.8 is a plot of the channel suppression at 10 Mb/s.

After tuning the channel separation network, the system was operated at 600 Mb/s. Figure 4.9 is a plot of the channel suppression at 600 Mb/s. Channel separation network performance was limited by frequency dependent gain and phase variations between the signals at each receiver array element. These variations were caused by component mismatches between the two receiver channels and by the multipath signals inherent in an indoor propagation environment. Given these channel mismatches, the channel suppression ratio is 12 dB (Table 4.3).

Receiver eye patterns are shown in Figure 4.10. Bit error rate (BER) measurements were performed offline on signals captured by the oscilloscope (Table 4.3). Measurements were made with both transmitters active and with only one transmitter active at a time. There was no measurable difference in the system BER for the two operating modes.

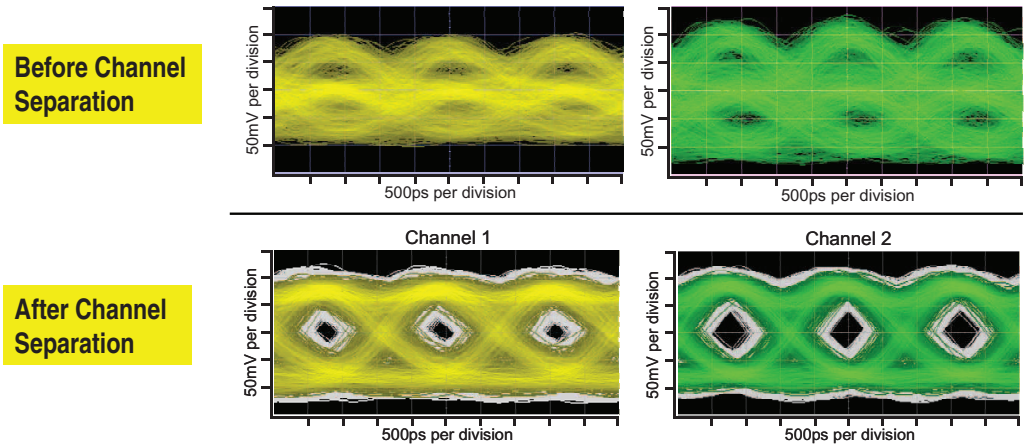

Figure 4.10: Measured eye patterns before and after channel separation (indoor link)

4.3.2 Outdoor Results

The hardware prototype was tested in an outdoor environment at a range of 41 m (Figure 4.11). The transmitter and receiver antenna pairs were separated by 32 cm. The receiver antennas were aimed using two-dimension tilt adjusters. Figure 4.12 shows channel separation network performance at 10 Mb/s data rate. The network was manually tuned to suppress cross-channel interference. Over a 60 MHz bandwidth, a 29 dB maximum channel suppression was achieved. Channel suppression levels for the two channels were within 1 dB at this data rate.

The operating data rate was then increased to 600 Mb/s (Figure 4.13). Over a 600 MHz bandwidth, cross-channel interference of channel 1 by channel 2 was suppressed by 21 dB over the data bandwidth. Cross-channel interference of

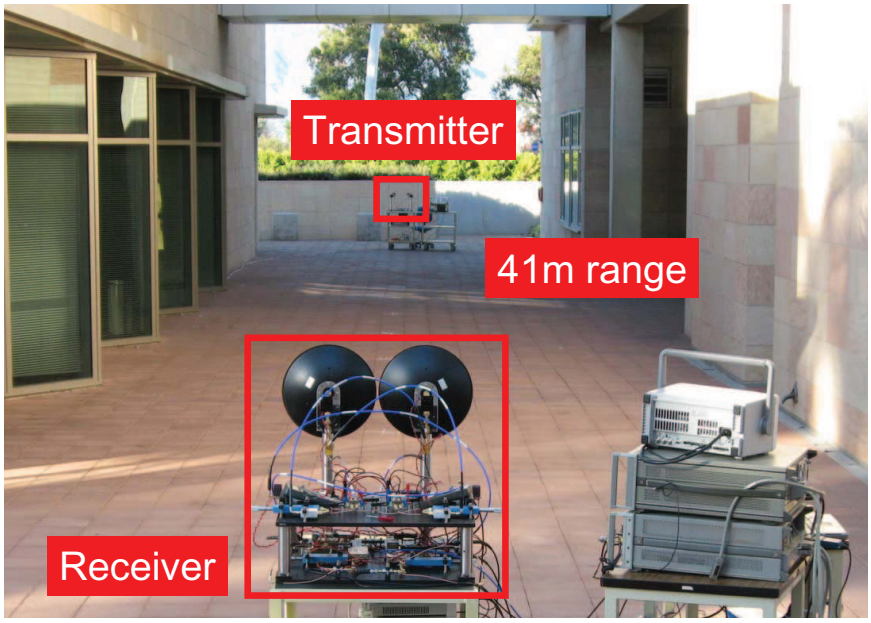

Figure 4.11: Outdoor radio link experiment

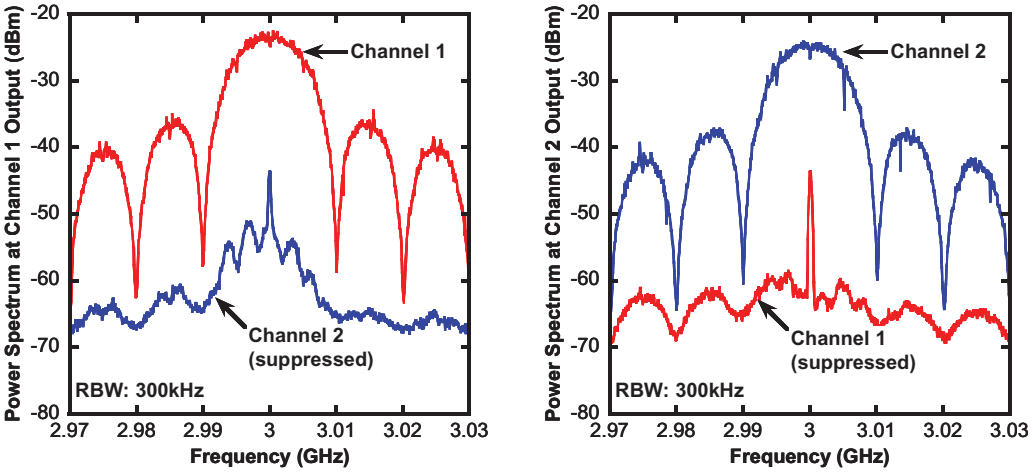

Figure 4.12: Outdoor channel separation network performance at 10 Mb/s

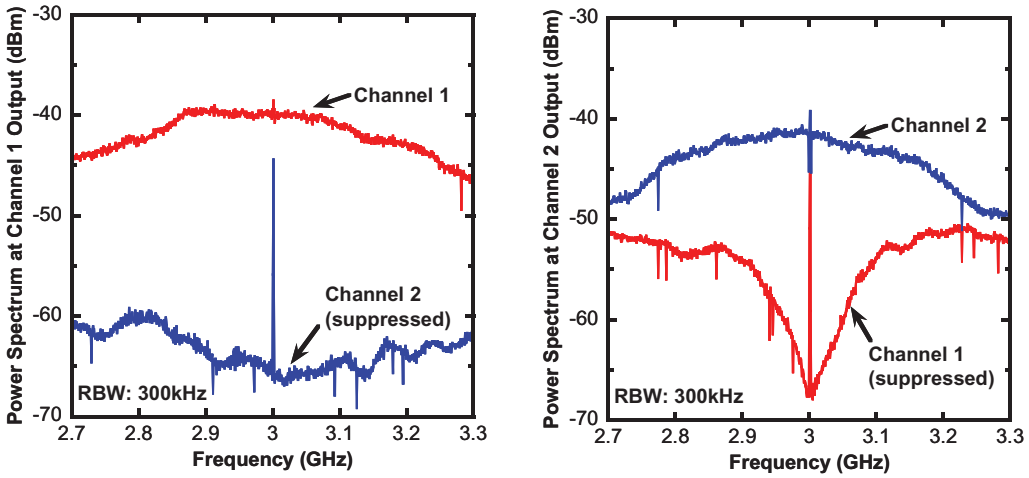

Figure 4.13: Outdoor channel separation network performance at 600 Mb/s

	Channel Number	1	2
BER	Single Active Transmitter	$< 10^{-6}$	$< 10^{-6}$
	Two Active Transmitters	$< 10^{-6}$	1.8×10^{-6}
Signal-to-Interference Ratio	10 Mb/s per channel	28 dB	29 dB
	600 Mb/s per channel	21 dB	10 dB

Table 4.4: Summary of outdoor measurements

channel 2 by channel 1 could be suppressed by only 10 dB. This is a consequence of a strong (and unintended) frequency-dependence to the gain or phase of the components within one summation branch of the channel separation network. Because of this, the cross-channel interference can only be nulled at the center of the IF bandwidth.

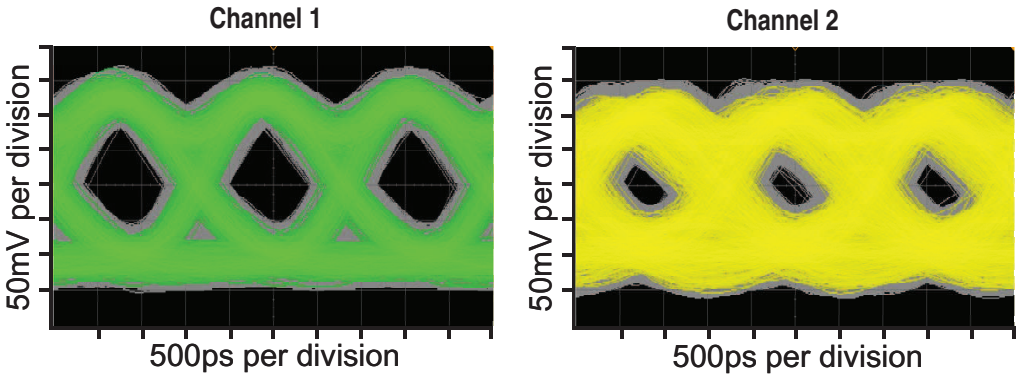

Figure 4.14: Measured eye patterns after channel separation (outdoor link)

Despite the limited suppression of the interference of channel 2 by channel 1, measured transmission BERs were better than 2×10^{-6} on both channels simultaneously (Table 4.4). To assess the impact of cross-channel interference on the transmission error rate, the system was tested with both transmitters active and with one transmitter active at a time. Measured BERs were $< 10^{-6}$ with only one active channel. Figure 4.14 shows the receiver eye patterns. The larger eye closure observed for channel 2 can be attributed to the lower suppression of cross-channel interference for channel 2 (Table 4.4).

4.4 Conclusions

This chapter described the design, implementation, and testing of a two-element hardware prototype using IF channel separation. Results from both in-

door and outdoor wireless testing have been presented and analyzed. These results are the first demonstrations of spatial multiplexing at millimeter-wave frequencies for both indoor and outdoor wireless links. This work strongly influenced the design of a four-element hardware prototype that is described in the next chapter.

Chapter 5

Four-Element Prototype: Adaptive Baseband Channel Separation

This chapter describes a four-element hardware prototype that was built to demonstrate adaptive baseband channel separation. Experimental results from indoor link testing are presented.

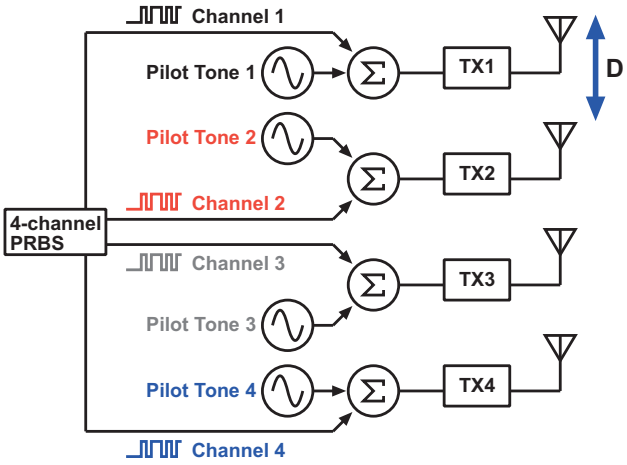

(a) Transmitter prototype

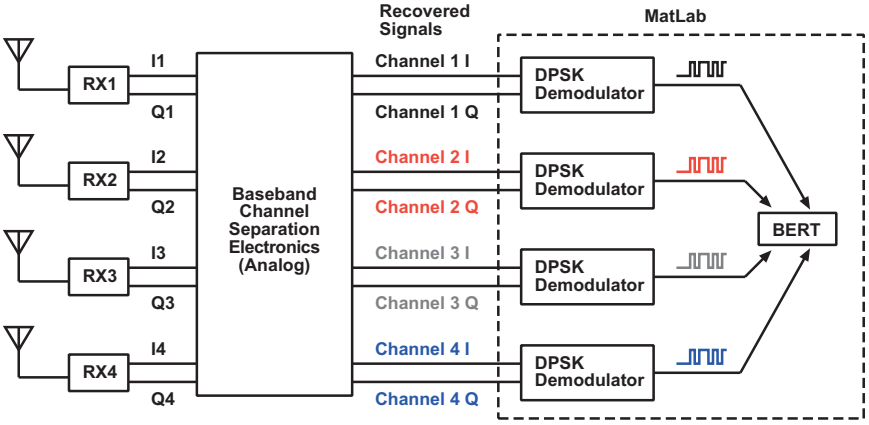

(b) Receiver prototype

Figure 5.1: Four-element hardware prototype

5.1 Prototype Design and Construction

The hardware prototype (Figure 5.1) used commercially available millimeter-wave and RF components and a printed circuit board based channel separation network. A control loop continuously tuned the channel separation network. Baseband channel separation was chosen to demonstrate a system architecture capable of scaling to larger array dimensions and higher aggregate system data rates.

The prototype consisted of a four-element transmitter and a four-element receiver. Section 5.1.1 describes the transmitter array prototype. The receiver array is described in Section 5.1.2, the receiver channel separation network is presented in Section 5.1.3, and the adaptive control loop is covered in Section 5.1.4.

5.1.1 Transmitter Array

The transmitter prototype (Figure 5.2) consisted of an FPGA baseband data source, pilot tone sources, BPSK modulators, and 60 GHz upconverters. An FPGA generated four independent Pseudo Random Bit Sequences (PRBS) at 600 Mb/s with sequence lengths $2^{20} - 1$, $2^{22} - 1$, $2^{23} - 1$, and $2^{25} - 1$. Each PRBS sequence had a different shift register length to conclusively show the receiver separates channels correctly. Unique pilot tones were added to each PRBS sequence and the combined signal was applied, in bipolar format, to the baseband port of

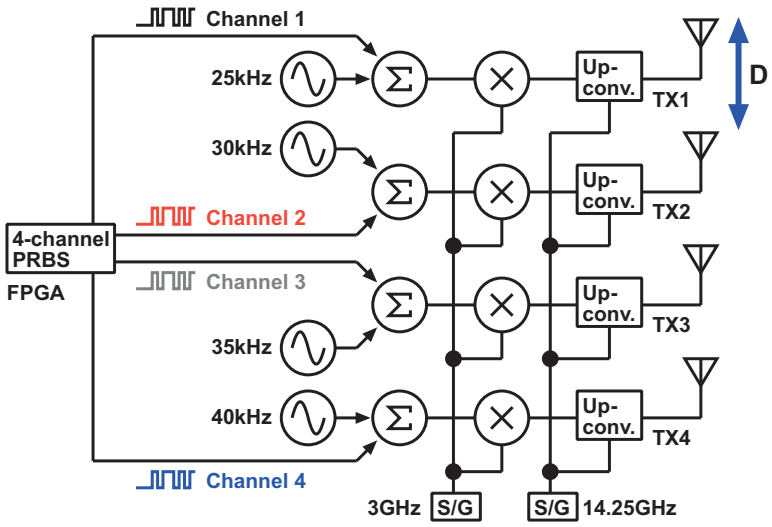

Figure 5.2: Transmitter prototype

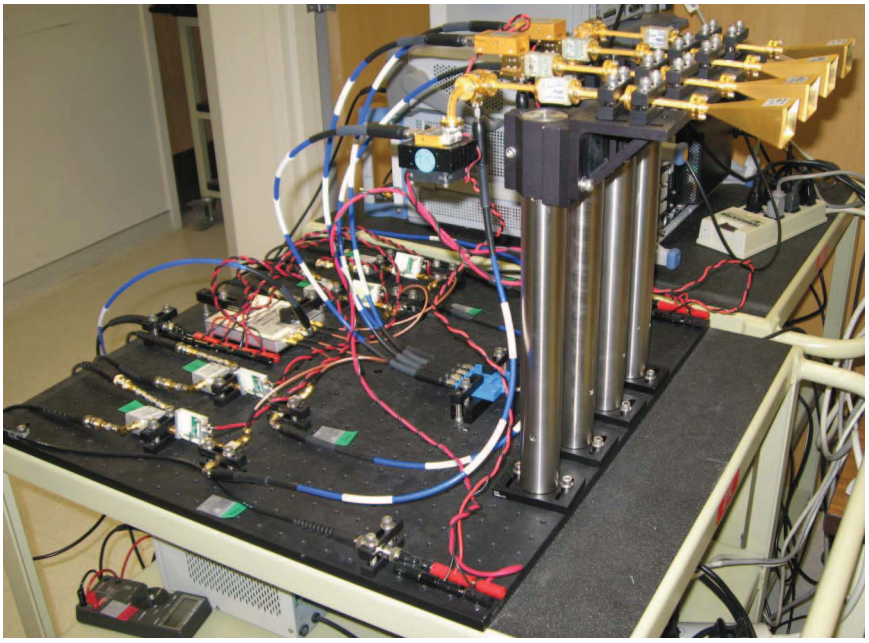

Figure 5.3: Photograph of the transmitter prototype

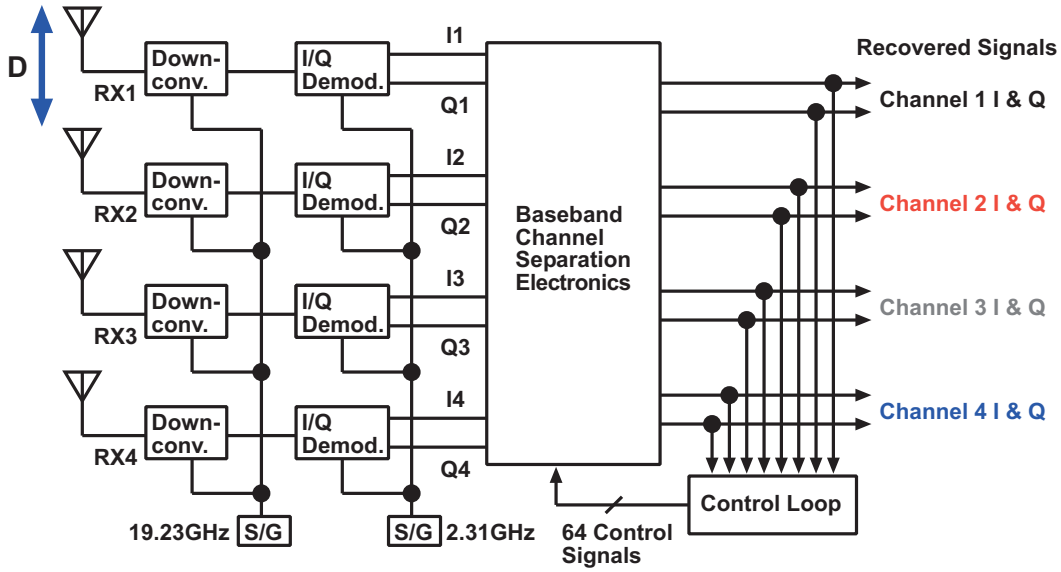

Figure 5.4: Receiver prototype

a mixer operating with a 3 GHz local oscillator. A second mixer upconverted the 3 GHz BPSK signal to 60 GHz. The mixer image response and LO feedthrough were both suppressed by a 58-62 GHz bandpass filter. Each transmitter used a 24 dB_i standard gain horn antenna (Figure 5.3). The antennas had a 7.9 cm spacing for the 5 m range indoor wireless link experiment.

5.1.2 Receiver Array

The receiver prototype (Figure 5.4) included 60 GHz downconverters, *I/Q* demodulators, baseband channel separation electronics, and a control loop. The 60 GHz downconverter modules brought the received signals down to a 2.31 GHz IF

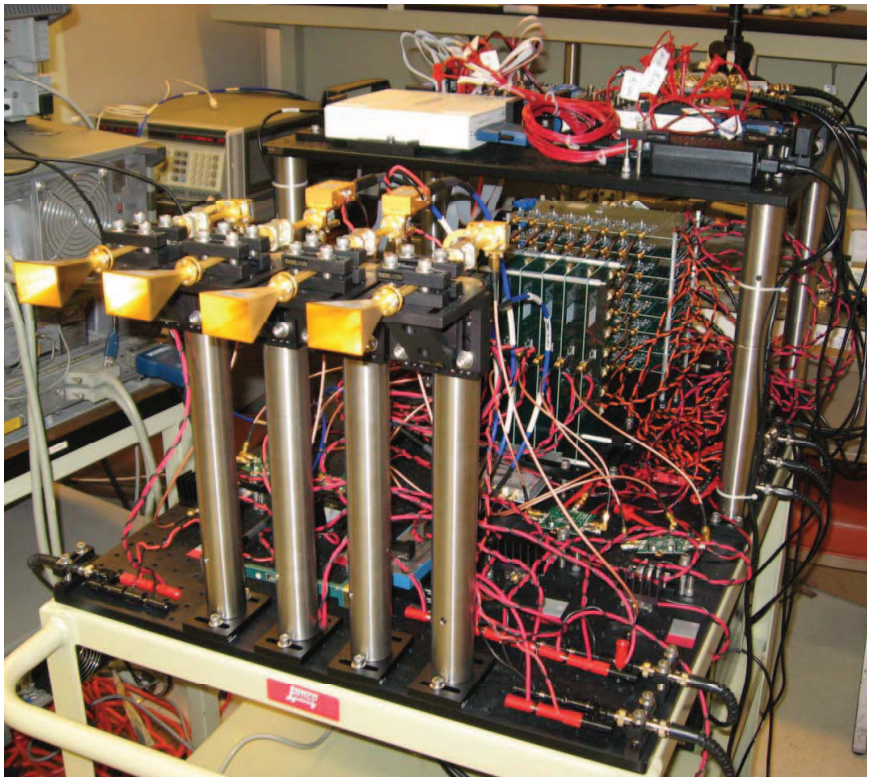

Figure 5.5: Photograph of the receiver prototype

frequency. They each consisted of a 24 dB_i standard gain horn antenna, bandpass filter, and a mixer (Figure 5.5). *I/Q* demodulators bring the received signals down to baseband. The antennas had a 7.9 cm spacing for the 5 m range indoor wireless link experiment. Signal splitters distribute the baseband I and Q signals to eight channel separation circuit boards (Section 5.1.3). Each PCB recovers either the I or Q component of a single channel.

The recovered data was captured on a two-channel oscilloscope controlled by a computer. The I and Q components of one recovered channel were simultaneously stored for offline bit error rate (BER) analysis. Carrier recovery was not implemented at the receiver. Final data recovery was performed offline by DPSK demodulation. This hardware prototype was capable of recovering all four channels simultaneously.

5.1.3 Receiver Channel Separation Network

The channel separation PCBs (Figure 5.6) consist of arrays of variable gain amplifiers (VGAs) and a summation network. Each VGA was a full four-quadrant analog multiplier, allowing arbitrary magnitude scaling and phase shift operations on each of the received signals. The summation network was an 8:1 resistor power combiner matched to 50 Ω. Transistor array ICs were used to implement the four quadrant analog multipliers (Figure 5.7). This design forced several compromises

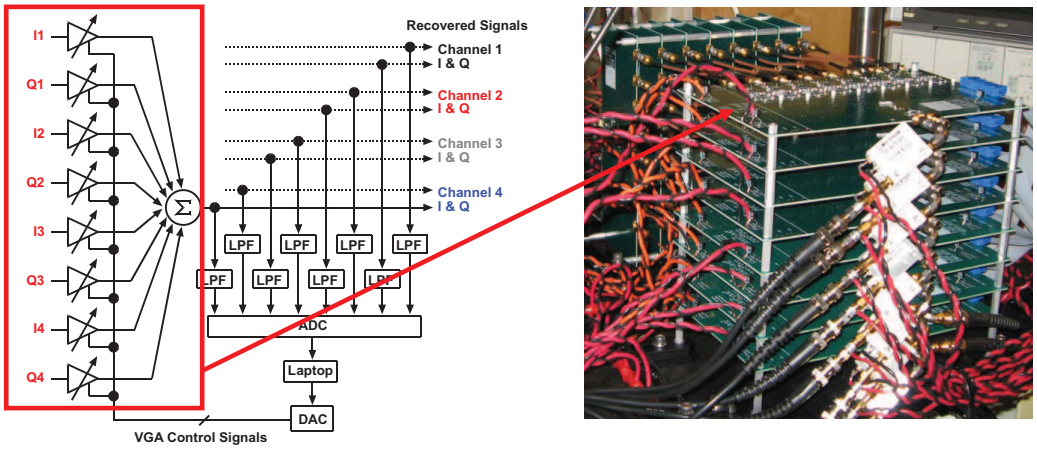

Figure 5.6: Receiver channel separation network

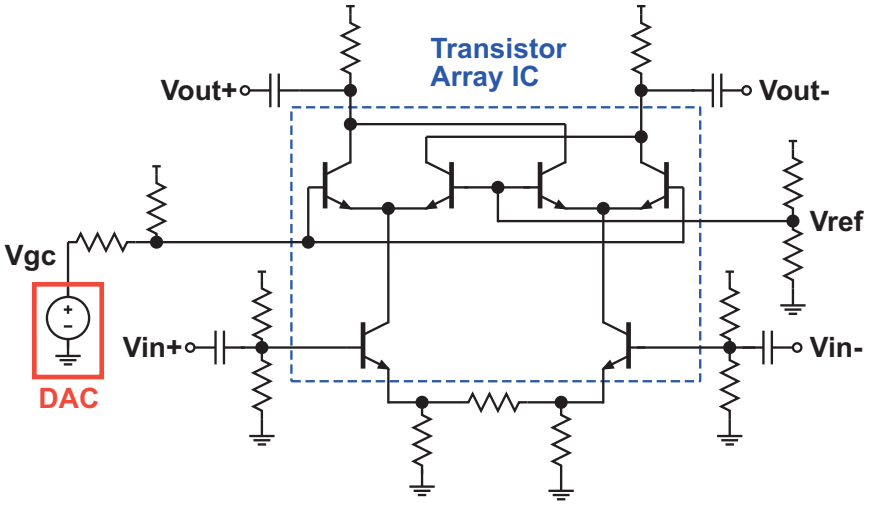

Figure 5.7: Discrete component four quadrant analog multiplier

compared to a custom IC implementation (Figure 3.10). Resistor biasing was used to reduce the component count. 64 copies of the circuit are required to implement the channel separation network. The circuit was AC coupled to avoid DC bias mismatches between circuits within the channel separation network. The gain control circuit used a reduced component count.

This compromise resulted in a nonlinear gain control curve that was sensitive to transistor beta and DC operating point variations. The circuit was simulated over the range of expected beta variation for the specified resistor tolerance to ensure that the gain control curve remained within the output voltage range of the DACs chosen for the control loop.

The nonlinear behavior and variations in the gain control curve limited the possible control loop algorithms. A gradient descent algorithm (Section 5.1.4) was chosen because the algorithm only requires a monotonic gain control function.

For an ideal system, only phase shift operations are required to separate channels at the receiver. A real system will have gain mismatches between individual transmitters and receivers and will also require magnitude scaling. The channel separation network must also be capable of arbitrary phase shift operations to account for antenna positioning and alignment errors.

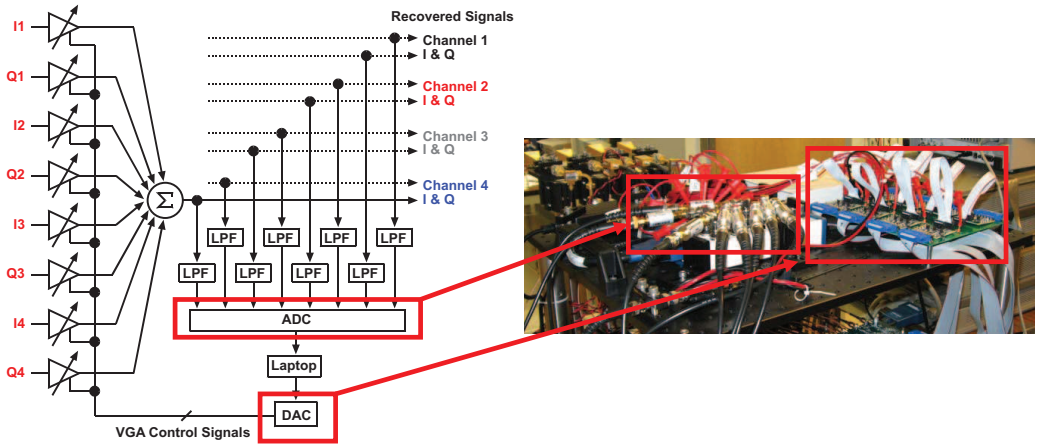

Figure 5.8: Receiver channel separation network control loop

5.1.4 Receiver Control Loop

The control loop (Figure 5.8) adjusted the baseband VGA coefficients so that the output of the channel separation network contains the data stream from the desired transmit channel, while canceling other interfering channels. First, the eight outputs of the channel separation network were filtered and digitized at 125 Ksamples/s to measure the magnitude of the embedded transmitter pilot tones (Figure 5.9). The sampling rate was determined not by the data rate, but by the pilot frequencies, which were 25 KHz, 30 KHz, 35 KHz, and 40 KHz, for transmitter channels 1, 2, 3, and 4, respectively. These frequencies were sufficiently higher than the lower cut-off frequency of the receiver chain (approximately 1 KHz),

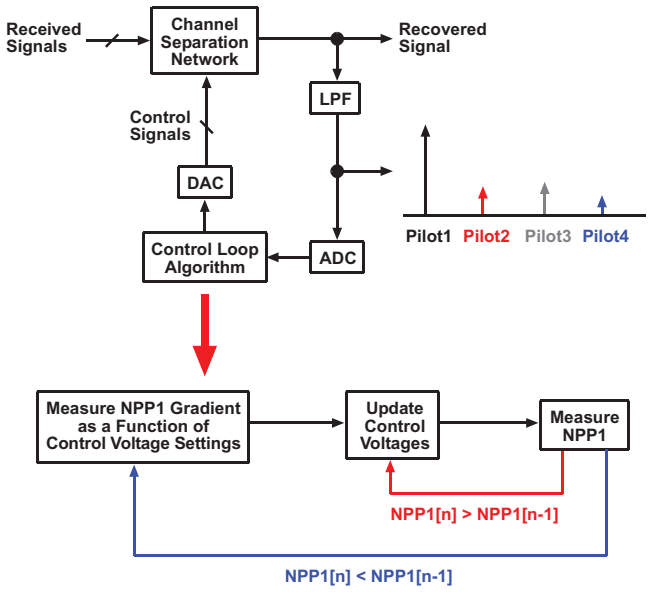

Figure 5.9: Control loop algorithm

but low enough to allow the use of low-cost multi-channel digitizers, regardless of actual data rate.

By performing an FFT operation, the magnitude of each pilot tone can be identified. Specifically, the amount of interference channel power at receiver k can be quantified by

$$NPP_k = \frac{P_{k,k}}{P_{k,1} + P_{k,2} + P_{k,3} + P_{k,4}}, \tag{5.1}$$

where NPP_k is the normalized pilot power at receiver k and $P_{k,j}$ is the pilot power from transmitter j coupled to the receiver k. It follows $0 \leq NPP_k \leq 1$, with the maximum achieved upon perfect channel separation with $P_{k,j} = 0$ for all $k \neq j$.

SIR at the receiver k can be estimated by

$$SIR_k = \frac{1}{\frac{1}{NPP_k} - 1}. \tag{5.2}$$

The control loop attempts to find the optimum tuning of the *k-th* receiver channel separation network, $\boldsymbol{c_{k,opt}}$, by maximizing the normalized pilot power,

$$\mathbf{c_{k,opt}} = arg_{\mathbf{c_k}} max NPP_k, \tag{5.3}$$

where $\boldsymbol{c_k} = [c_{1,I}\ c_{1,Q}\ c_{2,I}\ c_{2,Q}\ \ c_{4,I}\ c_{4,Q}]$ represents control voltages for the VGA array at receiver k. The optimization was implemented as a simple gradient-based iteration.

First, all VGA voltages are initialized, and the *k-th* channel gradient vector $\triangle \boldsymbol{c_k}$ is obtained by applying a small perturbation to each element of the vector $\boldsymbol{c_k}$. Next, an adjustment is made to voltage vectors to move along the direction of increasing NPP_k,

$$c_k^{(n+1)} = c_k^{(n)} + \beta \cdot \triangle c_k, \tag{5.4}$$

where $c_k^{(n+1)}$ and $c_k^{(n)}$ are *k-th* channel voltage vectors at *(n+1)-th* and *n-th* iteration, respectively. The amount of adjustment can be controlled by β, which is typically a small constant. Similar updates continue until NPP_k no longer increases, at which point the gradient $\triangle \boldsymbol{c_k}$ needs to be updated.

A single update of all four-channel VGA voltages required approximately 1 second, allowing for the tracking of slow-varying channel conditions and group

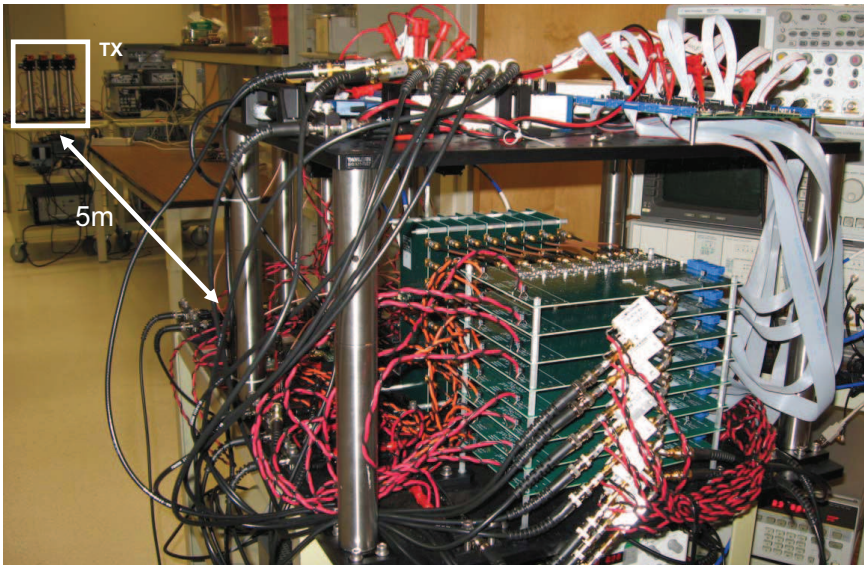

Figure 5.10: Indoor radio link experiment

delay variations in the receiver electronics. The loop speed was mainly limited by the programming time of the 64-channel D/A converter board, and could be improved by adopting a faster digital interface.

In the steady-state, typical measured NPP_k is 0.99, yielding ∼20 dB of SIR. The loop performance can also be enhanced by adopting various linear estimation techniques (e.g. [48]). The performance of the adaptive channel-separation loop is ultimately limited by random gaussian noise.

TX Antenna Gain	24	dB_i
RX Antenna Gain	24	dB_i
RX Power	5	m
Free-Space Path Loss	82	dB
RX Noise Figure	14	dB
BER	10^{-6}	
Link Margin	16	dB
TX Power	-10	dBm
RX Power	-44	dBm

Table 5.1: Link Budget

5.2 Experimental Results

The hardware prototype (Figure 5.10) was tested in an indoor office environment at a 5 m link range. The antenna element spacing was 7.9 cm at both the transmitter and receiver. Table **??** summarizes the prototype system link budget.

System performance was characterized in the frequency domain and with BER testing. The I and Q components of one recovered channel were simultaneously captured using a two-channel oscilloscope. DPSK data demodulation and BER measurements were performed offline on the captured signals.

5.2.1 Channel Separation Performance

Channel separation network performance was characterized in the frequency domain by transmitting 600 Mb/s PRBS sequences. After programming the con-

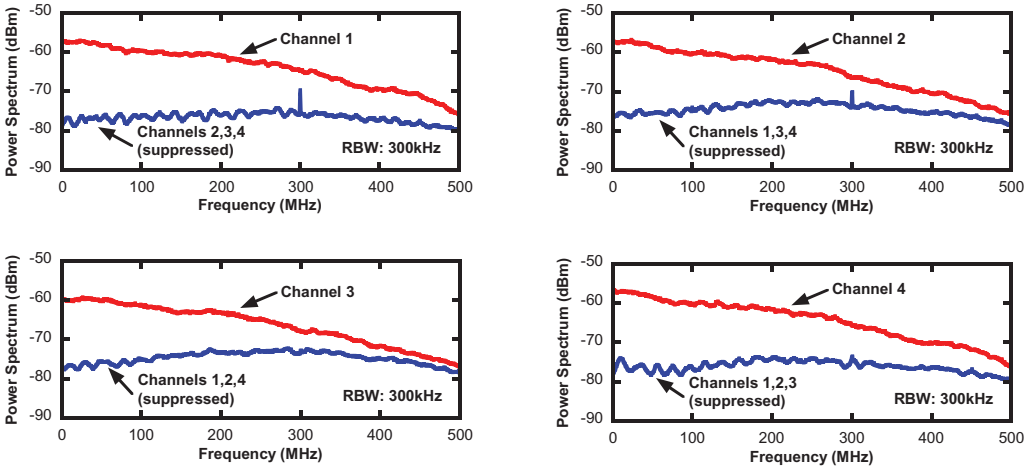

Figure 5.11: Measured channel separation network performance

trol loop to recover a particular channel, the received power spectrum was measured at the output of the channel separation network under two conditions. First, the desired channel was activated. The second measurement was made with the desired channel turned off and the three interference channels activated. Figure 5.11 shows the received power spectrum for each channel for both cases. The measured SIR for each channel is summarized in Table 5.2.

Similar performance was achieved for channels 1 and 4. Reduced channel 3 SIR levels can be attributed to the reduced power of the recovered signal relative to the other channels Figure 5.11.

Measurements of the output power of the 60 GHz upconverters varied by 0.4 dB across the transmitter array. Additional measurements are required to

determine the effect of multipath signal propagation on the measured variations in SIR performance.

5.2.2 Bit Error Rate Testing

Time domain testing was performed using 600 Mb/s PRBS signals. The BER performance of the system was measured for two cases. First, a single channel was activated and the BER was measured to obtain the system performance in the absence of interference signals. The second set of BER measurements was performed with all channels active simultaneously to assess the impact of channel separation network performance on transmission error rates.

For the case of a single active channel, the measured BER was $< 10^{-6}$ for all channels. BER measurement results for the case of all channels active simultaneously are summarized in Table 5.2. Similar performance was achieved for each recovered channel in both the presence and absence of interference signals, with the exception of channel 3. The increase in channel 3 BER in the presence of interference signals can be attributed to reduced SIR performance, compared to channels 1,2, and 4. These results are similar to the performance of a two-channel hardware prototype operating at 600 Mb/s per channel [32],[33]. Figure 5.12 shows typical receiver eye patterns after channel separation and DPSK demodulation. The eye patterns were generated offline on data captured for BER

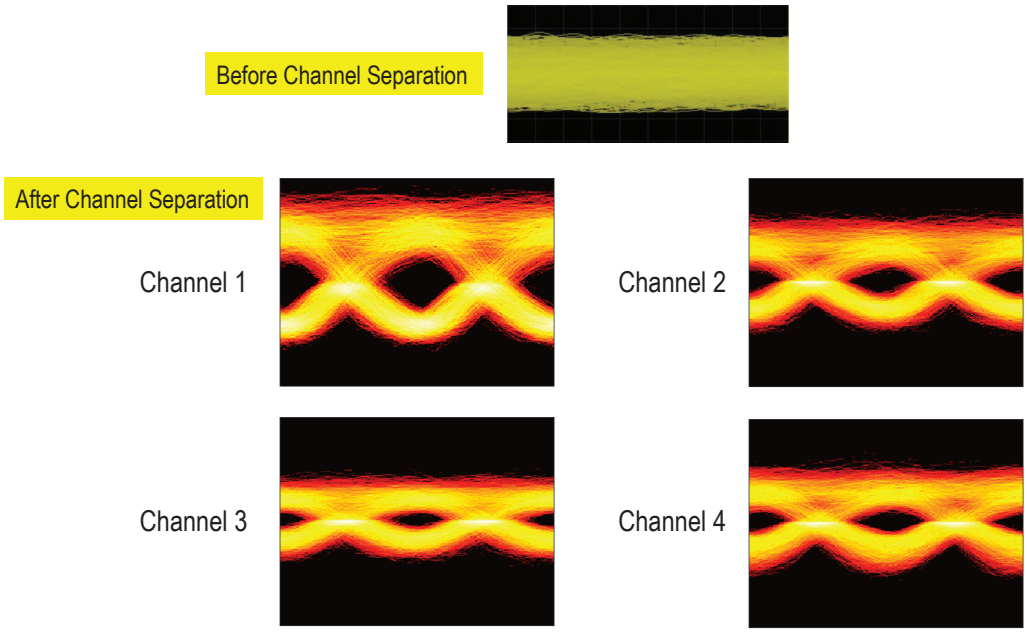

Figure 5.12: Receiver eye patterns before and after channel separation and offline DPSK demodulation

Recovered Channel	BER	Signal-to-Interference Ratio (dB)
1	$< 10^{-6}$	15
2	$< 10^{-6}$	12
3	1.2×10^{-5}	10
4	$< 10^{-6}$	14

Table 5.2: Summary of experimental results

measurements. Variations in eye closure can be attributed to the measured SIR performance of each channel (Table 5.2).

5.3 Conclusions

This chapter described the design, implementation, and testing of a four-element hardware prototype using adaptive baseband channel separation. Results from indoor wireless testing have been presented and analyzed. These results are the first demonstrations of adaptive spatial multiplexing at millimeter-wave frequencies.

Chapter 6

Conclusions

This dissertation presents the first experimental demonstration of a millimeter-wave line-of-sight communication link using spatial multiplexing. In this chapter, key achievements are summarized and suggestions for future work are presented.

6.1 Achievements

A comprehensive analysis of line-of-sight wireless links using spatial multiplexing was presented from a hardware perspective. Link sensitivity to non-ideal system installation, multipath signal propagation, and atmospheric refraction was analyzed. Channel separation network hardware implementations were proposed and simulated to determine performance tradeoffs.

A scalable system architecture for adaptive Line-of-Sight spatial multiplexing for millimeter-wave communication links was proposed and demonstrated. A key feature of this system architecture is the ability to decouple channel separation from other receiver functions such as carrier recovery and data demodulation.

Results from a two-element prototype using manually tuned channel separation hardware placed at the receiver IF frequency were presented. This work is the first demonstration of line-of-sight spatial multiplexing at millimeter-wave frequencies. The system achieved an aggregate system data rate of 1.2 Gb/s for both indoor and outdoor links operating at 6 m and 41 m link ranges, respectively.

A four-element baseband channel separation hardware prototype was presented. This prototype used adaptive channel separation to achieve a 2.4 Gb/s aggregate system data rate over a 5 m link range. This work demonstrated the scalability of the proposed system architecture and is the first demonstration of line-of-sight spatial multiplexing using adaptive baseband channel separation.

6.2 Future Work

The hardware prototype can be improved in several ways. Higher bandwidths and a reduction in hardware cost can be achieved by using custom ICs rather than the off-the-shelf components that were employed. Testing over link ranges

on the order of 1 km is needed to verify that the system architecture is capable of adapting to time varying atmospheric conditions. Prototypes using 4×4 arrays are needed to verify the theoretical link performance presented in this dissertation.

The channel separation control loop can be sped up by using a faster digital interface. Further work is needed to optimize the control loop algorithm to maximize channel separation network performance.

Dual polarization can be employed to further increase the system's multiplexing gain. DPSK can be replaced by coherent communication using larger alphabets (e.g., 16-QAM), with carrier synchronization performed at baseband after channel separation, using digital, or hybrid analog-digital, signal processing.

Recent advances in CMOS IC design indicate that a digital channel separation network is feasible. A CMOS IC featuring four 20 GS/s ADCs and a DSP capable of 12 trillion operations per second has been reported [1]. This IC was used to demonstrate a 40 Gb/s coherent optical communication link. The IC is a custom mixed-signal 20 million gate ASIC manufactured in 90 nm CMOS. The circuit dissipates 21 W.

Based on this result, the analog circuit based channel separation network presented in this dissertation could be replaced with an IC that features eight on chip ADCs and a DSP based channel separation network capable of > 20 trillion operations per second, sufficient for separating 4 channels each carrying 10 Gb/s.

This IC would consume approximately 40 W, a reasonable power consumption for an outdoor link connected to the local power grid.

SiBeam has recently introduced transmit and receive modules operating at 4 Gb/s using a 60 GHz carrier [30]. The modules cost approximately $800 and consume > 9 W and operate over a 10 m range [31]. The SiBeam system consumes approximately 2 nJ/W. A 40 Gb/s link using mixed signal channel separation may consume on the order of 1 nJ/W.

DSP based channel separation networks have several advantages over analog circuit based implementations. Performance is less sensitive to integrated circuit process variations. Analog circuit based channel separation ICs would require careful attention to layout in order to minimize on chip cross channel interference. Detailed circuit simulations are required to determine power and performance tradeoffs between analog and mixed signal channel separation networks.

Bibliography

[1] Sun, H. and Wu, K.-T. and Roberts, K, "Real-time measurements of a 40 Gb/s coherent system," *Optics Express*, vol. 16, no. 2, pp. 873–879, Jan 2008.

[2] M. Zargari, L. Nathawad, H. Samavati, S. Mehta, A. Kheirkhahi, P. Chen, K. Gong, B. Vakili-Amini, J. Hwang, S.-W. Chen, M. Terrovitis, B. Kaczynski, S. Limotyrakis, M. Mack, H. Gan, M. Lee, R. Chang, H. Dogan, S. Abdollahi-Alibeik, B. Baytekin, K. Onodera, S. Mendis, A. Chang, Y. Rajavi, S.-M. Jen, D. Su, and B. Wooley, "A Dual-Band CMOS MIMO Radio SoC for IEEE 802.11n Wireless LAN," *Solid-State Circuits, IEEE Journal of*, vol. 43, no. 12, pp. 2882–2895, Dec. 2008.

[3] P. Petrus, Q. Sun, S. Ng, J. Cho, N. Zhang, D. Breslin, M. Smith, B. McFarland, S. Sankaran, J. Thomson, R. Mosko, A. Chen, T. Lu, Y.-H. Wang, X. Zhang, D. Nakahira, Y. Li, R. Subramanian, A. Venkataraman, P. Kumar, S. Swaminathan, J. Gilbert, W. J. Choi, and H. Ye, "An Integrated Draft 802.11n Compliant MIMO Baseband and MAC Processor," pp. 266–602, Feb. 2007.

[4] A. Behzad, K. Carter, E. Chien, S. Wu, M. Pan, C. Lee, T. Li, J. Leete, S. Au, M. Kappes, Z. Zhou, D. Ojo, L. Zhang, A. Zolfaghari, J. Castanada, H. Darabi, B. Yeung, R. Rofougaran, M. Rofougaran, J. Trachewsky, T. Moorti, R. Gaikwad, A. Bagchi, J. Rael, and B. Marhoiev, "A Fully Integrated MIMO Multi-Band Direct-Conversion CMOS Transceiver for WLAN Applications (802.11n)," pp. 560–622, Feb. 2007.

[5] A. Hirata, T. Kosugi, H. Takahashi, R. Yamaguchi, F. Nakajima, T. Furuta, H. Ito, H. Sugahara, Y. Sato, and T. Nagatsuma, "120-GHz-band millimeter-wave photonic wireless link for 10-Gb/s data transmission," *Microwave Theory and Techniques, IEEE Transactions on*, vol. 54, no. 5, pp. 1937–1944, May 2006.

[6] T. Kosugi, A. Hirata, T. Nagatsuma, and Y. Kado, "MM-wave long-range wireless systems," *Microwave Magazine, IEEE*, vol. 10, no. 2, pp. 68–76, April 2009.

[7] V. Dyadyuk, J. Bunton, J. Pathikulangara, R. Kendall, O. Sevimli, L. Stokes, and D. Abbott, "A Multigigabit Millimeter-Wave Communication System With Improved Spectral Efficiency," *Microwave Theory and Techniques, IEEE Transactions on*, vol. 55, no. 12, pp. 2813–2821, Dec. 2007.

[8] Proxim Wireless Co. Homepage, `http://www.proxim.com`.

[9] Loea Corp. Homepage, `http://www.loeacom.com`.

[10] B. Floyd, S. Reynolds, U. Pfeiffer, T. Zwick, T. Beukema, and B. Gaucher, "SiGe bipolar transceiver circuits operating at 60 GHz," *Solid-State Circuits, IEEE Journal of*, vol. 40, no. 1, pp. 156–167, Jan. 2005.

[11] B. Heydari, M. Bohsali, E. Adabi, and A. Niknejad, "Millimeter-Wave Devices and Circuit Blocks up to 104 GHz in 90 nm CMOS," *Solid-State Circuits, IEEE Journal of*, vol. 42, no. 12, pp. 2893–2903, Dec. 2007.

[12] C. Doan, S. Emami, A. Niknejad, and R. Brodersen, "Millimeter-wave CMOS design," *Solid-State Circuits, IEEE Journal of*, vol. 40, no. 1, pp. 144–155, Jan. 2005.

[13] M. Khanpour, K. Tang, P. Garcia, and S. Voinigescu, "A Wideband W-Band Receiver Front-End in 65-nm CMOS," *Solid-State Circuits, IEEE Journal of*, vol. 43, no. 8, pp. 1717–1730, Aug. 2008.

[14] T. Yao, M. Gordon, K. Tang, K. Yau, M.-T. Yang, P. Schvan, and S. Voinigescu, "Algorithmic Design of CMOS LNAs and PAs for 60-GHz Radio," *Solid-State Circuits, IEEE Journal of*, vol. 42, no. 5, pp. 1044–1057, May 2007.

[15] B. Razavi, "A 60-GHz CMOS receiver front-end," *Solid-State Circuits, IEEE Journal of*, vol. 41, no. 1, pp. 17–22, Jan. 2006.

[16] ——, "A Millimeter-Wave CMOS Heterodyne Receiver With On-Chip LO and Divider," *Solid-State Circuits, IEEE Journal of*, vol. 43, no. 2, pp. 477–485, Feb. 2008.

[17] X. Guan, H. Hashemi, and A. Hajimiri, "A fully integrated 24-GHz eight-element phased-array receiver in silicon," *Solid-State Circuits, IEEE Journal of*, vol. 39, no. 12, pp. 2311–2320, Dec. 2004.

[18] A. Natarajan, A. Komijani, X. Guan, A. Babakhani, and A. Hajimiri, "A 77-GHz Phased-Array Transceiver With On-Chip Antennas in Silicon: Transmitter and Local LO-Path Phase Shifting," *Solid-State Circuits, IEEE Journal of*, vol. 41, no. 12, pp. 2807–2819, Dec. 2006.

[19] A. Babakhani, X. Guan, A. Komijani, A. Natarajan, and A. Hajimiri, "A 77-GHz Phased-Array Transceiver With On-Chip Antennas in Silicon: Receiver and Antennas," *Solid-State Circuits, IEEE Journal of*, vol. 41, no. 12, pp. 2795–2806, Dec. 2006.

[20] T. Yu and G. Rebeiz, "A 2224 GHz 4-Element CMOS Phased Array With On-Chip Coupling Characterization," *Solid-State Circuits, IEEE Journal of*, vol. 43, no. 9, pp. 2134–2143, Sept. 2008.

[21] K.-J. Koh, J. May, and G. Rebeiz, "A Q-band (4045 GHz) 16-element phased-array transmitter in 0.18-?m SiGe BiCMOS technology," pp. 225–228, 17 2008-April 17 2008.

[22] H. Krishnaswamy and H. Hashemi, "A Fully Integrated 24GHz 4-Channel Phased-Array Transceiver in 0.13m CMOS Based on a Variable-Phase Ring Oscillator and PLL Architecture," pp. 124–591, Feb. 2007.

[23] M. Tanomura, Y. Hamada, S. Kishimoto, M. Ito, N. Orihashi, K. Maruhashi, and H. Shimawaki, "TX and RX Front-Ends for 60GHz Band in 90nm Standard Bulk CMOS," pp. 558–635, Feb. 2008.

[24] K. Maruhashi, M. Tanomura, Y. Hamada, M. Ito, N. Orihashi, and S. Kishimoto, "60-GHz-Band CMOS MMIC Technology for High-Speed Wireless Personal Area Networks," pp. 1–4, Oct. 2008.

[25] A. Tomkins, R. Aroca, T. Yamamoto, S. Nicolson, Y. Doi, and S. Voinigescu, "A Zero-IF 60 GHz 65 nm CMOS Transceiver With Direct BPSK Modulation Demonstrating up to 6 Gb/s Data Rates Over a 2 m Wireless Link," *Solid-State Circuits, IEEE Journal of*, vol. 44, no. 8, pp. 2085–2099, Aug. 2009.

[26] E. Laskin, P. Chevalier, A. Chantre, B. Sautreuil, and S. Voinigescu, "165-GHz Transceiver in SiGe Technology," *Solid-State Circuits, IEEE Journal of*, vol. 43, no. 5, pp. 1087–1100, May 2008.

[27] S. Nicolson, A. Tomkins, K. Tang, A. Cathelin, D. Belot, and S. Voinigescu, "A 1.2V, 140GHz receiver with on-die antenna in 65nm CMOS," pp. 229–232, 17 2008-April 17 2008.

[28] M. Seo, B. Jagannathan, C. Carta, J. Pekarik, L. Chen, C. Yue, and M. Rodwell, "A 1.1V 150GHz amplifier with 8dB gain and +6dBm saturated output power in standard digital 65nm CMOS using dummy-prefilled microstrip lines," pp. 484–485, Feb. 2009.

[29] Y. Palaskas, A. Ravi, S. Pellerano, B. R. Carlton, M. A. Elmala, R. Bishop, G. Banerjee, R. B. Nicholls, S. Ling, P. Seddighrad, S.-Y. Suh, S. S. Taylor, and K. Soumyanath, "A 5GHz, 108Mb/s 22 MIMO CMOS Transceiver," pp. 239–242, Jan. 2007.

[30] J. Gilbert, C. Doan, S. Emami, and C. Shung, "A 4-Gbps Uncompressed Wireless HD A/V Transceiver Chipset," *Micro, IEEE*, vol. 28, no. 2, pp. 56–64, March-April 2008.

[31] 60GHz Gains Traction at CES09, `http://www.eetimes.com/conf/ces/showArticle.jhtml?articleID=212800003& kc=5023& printable=true& printable=true`.

[32] E. Torkildson, B. Ananthasubramaniam, U. Madhow and M. Rodwell, "Millimeter-wave MIMO: Wireless Links at Optical Speeds," *(Invited Paper) Proc. of 44th Allerton Conference on Communication, Control and Computing, Monticello, Illinois*, Sept. 2006.

[33] F. Bohagen, P. Orten, and G. Oien, "Design of Optimal High-Rank Line-of-Sight MIMO Channels," *Wireless Communications, IEEE Transactions on*, vol. 6, no. 4, pp. 1420–1425, April 2007.

[34] ——, "Optimal Design of Uniform Planar Antenna Arrays for Strong Line-of-Sight MIMO Channels," pp. 1–5, July 2006.

[35] ——, "Modeling and analysis of a 40 GHz MIMO system for fixed wireless access," vol. 3, pp. 1691–1695 Vol. 3, May-1 June 2005.

[36] ——, "Construction and capacity analysis of high-rank line-of-sight MIMO channels," vol. 1, pp. 432–437 Vol. 1, March 2005.

[37] P. Larsson, "Lattice array receiver and sender for spatially orthonormal MIMO communication," *Vehicular Technology Conference, 2005. VTC 2005-Spring. 2005 IEEE 61st*, vol. 1, pp. 192–196 Vol. 1, May-1 June 2005.

[38] C. Sheldon, E. Torkildson, M. Seo, C. Yue, U. Madhow, and M. Rodwell, "A 60GHz line-of-sight 2x2 MIMO link operating at 1.2Gbps," pp. 1–4, July 2008.

[39] C. Sheldon, E. Torkildson, M. Seo, C. Yue, M. Rodwell, and U. Madhow, "Spatial multiplexing over a line-of-sight millimeter-wave MIMO link: A two-channel hardware demonstration at 1.2Gbps over 41m range," *Wireless Technology, 2008. EuWiT 2008. European Conference on*, pp. 198–201, Oct. 2008.

[40] C. Sheldon, M. Seo, E. Torkildson, M. Rodwell, and U. Madhow, "Four-Channel Spatial Multiplexing Over a Millimeter-Wave Line-of-Sight Link," *IEEE - MTTS International Microwave Symposium*, June 2009.

[41] S.O. Kasap, *Optoelectronics and Photonics*. Upper Saddle River, NJ: Prentice-Hall, 2001.

[42] D. Gesbert, H. Bolcskei, D. Gore, and A. Paulraj, "Outdoor MIMO wireless channels: models and performance prediction," *Communications, IEEE Transactions on*, vol. 50, no. 12, pp. 1926–1934, Dec 2002.

[43] U. Madhow, *Fundamentals of Digital Communication*. New York, NY: Cambridge University Press, 2008.

[44] J. Seybold, *Introduction to RF Propagation*. Hoboken, NJ: Wiley-Interscience, 2005.

[45] M. Thompson, L. Wood, H. Janes, and D. Smith, "Phase and amplitude scintillations in the 10 to 40 GHz band," *Antennas and Propagation, IEEE Transactions on*, vol. 23, no. 6, pp. 792–797, Nov 1975.

[46] C.F. Van Loan, *Introduction to Scientific Computing*, second edition ed. Upper Saddle River, NJ: Prentice-Hall, 2000.

[47] B. Gilbert, "A precise four-quadrant multiplier with subnanosecond response," *Solid-State Circuits, IEEE Journal of*, vol. 3, no. 4, pp. 365–373, Dec 1968.

[48] S. Haykin, *Adaptive Filter Theory*, fourth-edition ed. Upper Saddle River, NJ: Prentice-Hall, 2002.